

Methane seepage at Vestnesa Ridge (NW Svalbard) since the Last Glacial Maximum

Schneider A.^{1,*}, Panieri G.¹, Lepland A.^{1,2,8}, Consolaro C.^{1,3}, Cremiere A.^{2,4}, Forwick M.⁵, Johnson J. E.⁶, Plaza-Faverola A.¹, Sauer S.^{1,2,7}, Knies J.^{1,2}

¹ UiT Arctic Univ Norway, Dept Geosci, CAGE Ctr Arctic Gas Hydrate Environm & Climate, N-9037 Tromso, Norway.

² Geol Survey Norway, N-7491 Trondheim, Norway.

³ Plymouth Univ, Sch Geog Earth & Environm Sci, Plymouth PL4 8AA, Devon, England.

⁴ CALTECH, Div Geol & Planetary Sci, Pasadena, CA 91125 USA.

⁵ UiT Arctic Univ Norway, Dept Geosci, N-9037 Tromso, Norway.

⁶ Univ New Hampshire, Dept Earth Sci, Durham, NH 03824 USA.

⁷ Inst Francais Rech Exploitat Mer Ifremer, Dept Marine Geosci, Plouzane, France.

⁸ Tallinn Univ Technol, Dept Geol, Tallinn, Estonia.

* Corresponding author : A. Schneider, email address : andrea.schneider@uit.no

Abstract :

Multiple proxies in the geological record offshore NW Svalbard track shallow subseafloor diagenesis and seafloor methane seepage during the Last Glacial Maximum (LGM) extent and the disintegration of the Svalbard Barents Sea Ice Sheet (SBIS). Vestnesa Ridge, located at 79°N and in 1200 m water depth, is one of the northernmost known active methane seep sites and is characterised by a subseafloor fluid flow system, numerous seafloor pockmarks and gas flares in the water column. In this study, we develop a Late Pleistocene and Holocene stratigraphic framework, use stable oxygen and carbon isotope signatures ($\delta^{18}\text{O}$, $\delta^{13}\text{C}$) of benthic and planktic foraminifera, the mineralogical and carbon isotope composition of methane-derived authigenic carbonate (MDAC) and sediment geochemical data of ten sediment cores to assess methane seepage variability on Vestnesa Ridge.

The studied cores cover the age range between 31.9 and 10 cal ka BP and record 32 negative $\delta^{13}\text{C}$ excursions in benthic and planktic foraminifera with amplitudes down to -29% VPDB. These $\delta^{13}\text{C}$ excursions are often associated with elevated Ca/Ti and Sr/Ti elemental ratios in sediments and MDAC nodules. The precipitation of MDAC overgrowth on foraminiferal tests explains most of the negative $\delta^{13}\text{C}$ excursions. In this dataset, the oldest recorded methane emission episodes on Vestnesa Ridge occurred between the LGM (24–23.5 cal ka BP) and Heinrich Event 1 (HE 1; 17.7–16.8 cal ka BP).

Geological indicators for past subseafloor methane cycling and seafloor methane seepage, such as negative foraminiferal $\delta^{13}\text{C}$ excursions, MDAC nodules, and elevated Sr/Ti elemental ratios recorded in post-LGM sediments, possibly represent vertical migration of the sulphate-methane transition zone (SMTZ) and post-date sedimentation by up to 13.4 ka. However, it is important to note that indications of post-LGM seafloor methane seepage at Vestnesa Ridge also correspond to the established methane

efflux chronology for the adjacent Barents Sea shelf, implying that glacio-isostatic adjustments and associated re-activation of pre-existing deep-seated faults after disintegration of the SBIS are likely important controlling factors on fluid migration towards the seafloor.

Highlights

► Multiple proxies document diagenesis and methane seepage at Vestnesa Ridge since the LGM. ► Diagenetic alteration of foraminifera and MDAC precipitation may postdate the host sediment age by up to 13.4 ka. ► Timing of methane seepage corresponds to the LGM and deglaciation of the SBIS. ► Glacio-isostatic adjustments may be a key control on methane seepage.

Keywords : Micropaleontology, Foraminifers, Stable isotopes, Methane seepage, Authigenic carbonate, Holocene, Pleistocene, Paleogeography, Deglaciation, Arctic Ocean

59 1 Introduction

60 Current global warming raises concern about the role of methane, a powerful greenhouse gas, in the
61 Arctic as the circum-Arctic is expected to experience a larger temperature increase than any other
62 region on the planet (Serreze and Barry, 2011; IPCC, 2013; AMAP, 2015). In the upcoming century,
63 increasing Arctic bottom water temperatures are hypothesised as potential drivers for destabilisation
64 of gas hydrates along continental margins that may cause unprecedented release of methane into the
65 water column and the atmosphere (Reagan and Moridis 2007; Westbrook et al., 2009; Biastoch et al.,
66 2011; Giustiniani et al., 2013; Kretschmer et al., 2015; James et al., 2016). Although causal relationships
67 between recent climate warming and increased methane release from Arctic Ocean sediments may
68 seem likely, seepage observed today could have been initiated thousands of years ago. For example,
69 methane release on the East Siberian Arctic Shelf attributed to current global warming (Shakhova et
70 al., 2010) is more likely the result of submarine permafrost thaw after the inundation of terrestrial

71 permafrost during the Holocene marine transgression (Bauch et al. 2001; Dmitrenko et al., 2011). Also,
72 the persistent leakage of methane in the deep ocean offshore north-western Svalbard may not be
73 related to climate warming (Knies et al., 2018).

74 To evaluate if climate warming or other Earth system processes affect the release of methane stored
75 in Arctic Ocean sediments, a better understanding of the timing and drivers of past methane seepage
76 variability in the Arctic is required. Since active methane seepage at Vestnesa Ridge, western Svalbard
77 (Fig. 1), was first revealed by water column acoustic data, research in the area has provided key
78 information for understanding the dynamics of seafloor methane release and seepage over geological
79 time scales in the Arctic (Panieri et al. 2017b and references therein). Previous studies found evidence
80 for seepage occurring during the past 17 cal ka (Panieri et al., 2014; Consolaro et al., 2015; Ambrose
81 et al., 2015; Szybor and Rasmussen, 2017a; 2017b; Schneider et al., 2017). However, these
82 observations have limited regional coverage. The objective of this study is to identify episodes of past
83 methane seepage along Vestnesa Ridge since the Last Glacial Maximum (LGM) and during the retreat
84 of the Svalbard-Barents Sea Ice Sheet (SBIS). We develop a Late Pleistocene and Holocene stratigraphic
85 framework for the investigated sediment cores from Vestnesa Ridge, and correlate our sedimentary
86 record with established stratigraphic marker horizons along the western Svalbard continental margin.
87 We use multiple proxies such as $\delta^{18}\text{O}$ and $\delta^{13}\text{C}$ records from benthic and planktic foraminifera,
88 chemosynthetic bivalves, mineralogy and $\delta^{13}\text{C}$ of MDAC, and sediment geochemical data to identify
89 shallow subseafloor diagenesis and seafloor methane seepage. This study provides the first
90 comprehensive insight into timing and drivers of methane seepage activity or quiescence along
91 Vestnesa Ridge since the LGM.

92

93 2 Background and processes in gas-charged sediments

94 Methane (CH_4) can be of microbial, thermogenic, or abiotic origin (Whiticar, 1999) and occurs in
95 hydrocarbon reservoirs, stored in hydrate, or as dissolved and free gas in continental margin sediments
96 worldwide (Kretschmer et al., 2015; Ruppel and Kessler, 2017). Methane seepage occurs where fluids

97 enriched in methane migrate toward the sediment-water interface (e.g. Torres and Bohrmann, 2006;
98 Etiope, 2015). Seepage is commonly understood as the release of fluids from the seafloor on
99 continental margins and its location is named “seep” (Judd and Hovland, 2007 and references therein).
100 The geochemical conditions at methane seeps are characterised by opposing gradients of porewater
101 sulphate (SO_4^{2-}) and methane. A biogeochemical zone, the sulphate-methane transition zone (SMTZ),
102 is established close or up to several metres below the seafloor, where microbial co-metabolism
103 counterbalances the upward flux of methane and the downward flux of sulphate (Reeburgh, 1976;
104 Whiticar and Faber, 1986; Valentine, 2002; Tryon, et al. 1999). A changing methane flux can cause
105 vertical migration of the SMTZ through the sediment (Borowski et al., 1996). A key geochemical process
106 at the SMTZ (Eq. 1) is the microbially mediated anaerobic oxidation of methane (AOM) involving
107 syntrophic consortia of methane-oxidizing archaea and sulphate-reducing bacteria (Knittel and
108 Boetius, 2009 and references therein):

109



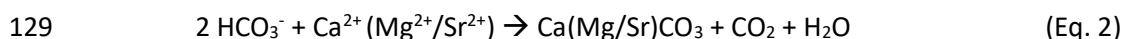
111

112 Reducing conditions at the SMTZ can result in reductive dissolution of magnetic Fe-oxides (Canfield
113 and Berner, 1987; Peckmann et al., 2001; Riedinger et al., 2005; Novosel et al., 2005; Dewangen et al.,
114 2013) and alteration of the initial sediment composition and magnetic properties due to replacement
115 of magnetic Fe-oxides by paramagnetic authigenic Fe-sulfides (Ferrell and Aharon, 1994; Bohrmann et
116 al., 1998; Rodriguez et al., 2000; Greinert et al., 2001; März et al., 2008; Lin et al., 2016; 2017). Barium
117 (Ba^{2+}) that is present dissolved in seep fluids (Hanor, 2000; Torres et al., 2003a) can react with
118 porewater sulphate and can precipitate as authigenic barite (BaSO_4) at the upper boundary of the
119 SMTZ (Torres et al., 1996, Dickens, 2001; Paytan et al., 2002; Riedinger et al., 2006; Kasten et al., 2012;
120 Sauer et al., 2017). As porewater sulphate is depleted underneath the SMTZ, buried barite dissolves
121 and barium diffuses upward to the SMTZ where it re-precipitates as authigenic barite (Torres et al.,
122 1996; Dickens, 2001). Barite fronts are commonly found immediately above the present-day depth of

123 porewater sulphate depletion (Dickens, 2001; Riedinger et al., 2006) and serve as a geochemical tracer
124 for the SMTZ.

125 The SMTZ is also the sedimentary interval where MDAC precipitates. The AOM (Eq. 1) elevates the
126 porewater alkalinity (Ritger et al., 1986; Paull et al., 1992), and thus promotes the precipitation of
127 $\text{Ca}(\text{Mg}/\text{Sr})\text{CO}_3$ (Eq. 2):

128



130

131 Carbonates with $\delta^{13}\text{C}$ values more negative than -30‰ VPDB are consistent with carbon sourced from
132 AOM (Whiticar, 1999; Aloisi et al., 2000; Bohrmann et al., 2001; Greinert et al., 2001; Naehr et al.,
133 2007). MDAC is often composed of aragonite, high-Mg calcite (5-20mol% MgCO_3 , Burton 1993), or
134 dolomite (Bohrmann et al., 1998; 2001; Aloisi et al., 2000; Greinert et al., 2001, Naehr et al., 2007) and
135 occur as early diagenetic micrite-cemented nodules, cavity fills, coatings, or crusts on the seafloor
136 (Bohrmann et al., 1998; 2002; Mazzini et al., 2004; Bayon et al., 2009; Crémière et al., 2016a; Sauer et
137 al., 2017). Aragonite and high-Mg calcite precipitate near the seafloor and indicate that the SMTZ was
138 located in the shallow subsurface (cm or dm scale) during episodes of high CH_4 -flux (Aloisi et al., 2000;
139 Greinert et al., 2001; Naehr et al., 2007). It was suggested that large MDAC crusts require time spans
140 of hundreds to thousands of years to form and often yield different ages compared to their host
141 sediment (Teichert et al., 2003; Bayon et al., 2009; Luff et al., 2004; 2005).

142 Together with fossil remains of seep fauna, MDAC provides direct geological evidence of AOM and
143 methane seepage in the sedimentary record. Panieri et al. (2017a) showed that foraminifera serve as
144 preferred nucleation templates for authigenic Mg-calcite precipitation at methane seeps. Negative
145 $\delta^{13}\text{C}$ excursions from benthic foraminifera in sedimentary records have been used to identify periodic
146 release of methane stored in gas hydrates at various times in earth history (Dickens, 1997; Kennet et
147 al., 2000; Thomas et al., 2002; Jenkyns et al., 2003; Tripathi and Elderfield, 2005; Zachos et al., 2007).

148 Several studies have shown that MDAC precipitates form coatings around foraminiferal tests and may

149 overprint the primary shell mineralogy and stable isotope composition, which complicates the use of
150 foraminiferal $\delta^{13}\text{C}$ records as past seepage archives (Rathburn et al. 2000; Torres et al., 2003b; 2010;
151 Martin et al., 2010; Panieri et al., 2009; 2014; 2017a; Consolaro et al., 2015; Schneider et al., 2017).

152

153 3 Study area

154 Vestnesa Ridge is located at 79°N on the western continental margin of the Svalbard Archipelago (Fig.
155 1 a; b). The ridge, in 1200-1300 m water depth, is approximately 100 km long and composed of > 2 km
156 thick Pliocene and Pleistocene sediments overlying < 20 million years (Ma) old oceanic crust (Eiken and
157 Hinz, 1993; Engen et al., 2008). The youngest sediments of Late Pleistocene and Holocene age are silty
158 turbidites, muddy-silty contourites, and hemipelagites (Vogt et al., 1994; 1999; Howe et al., 2008).

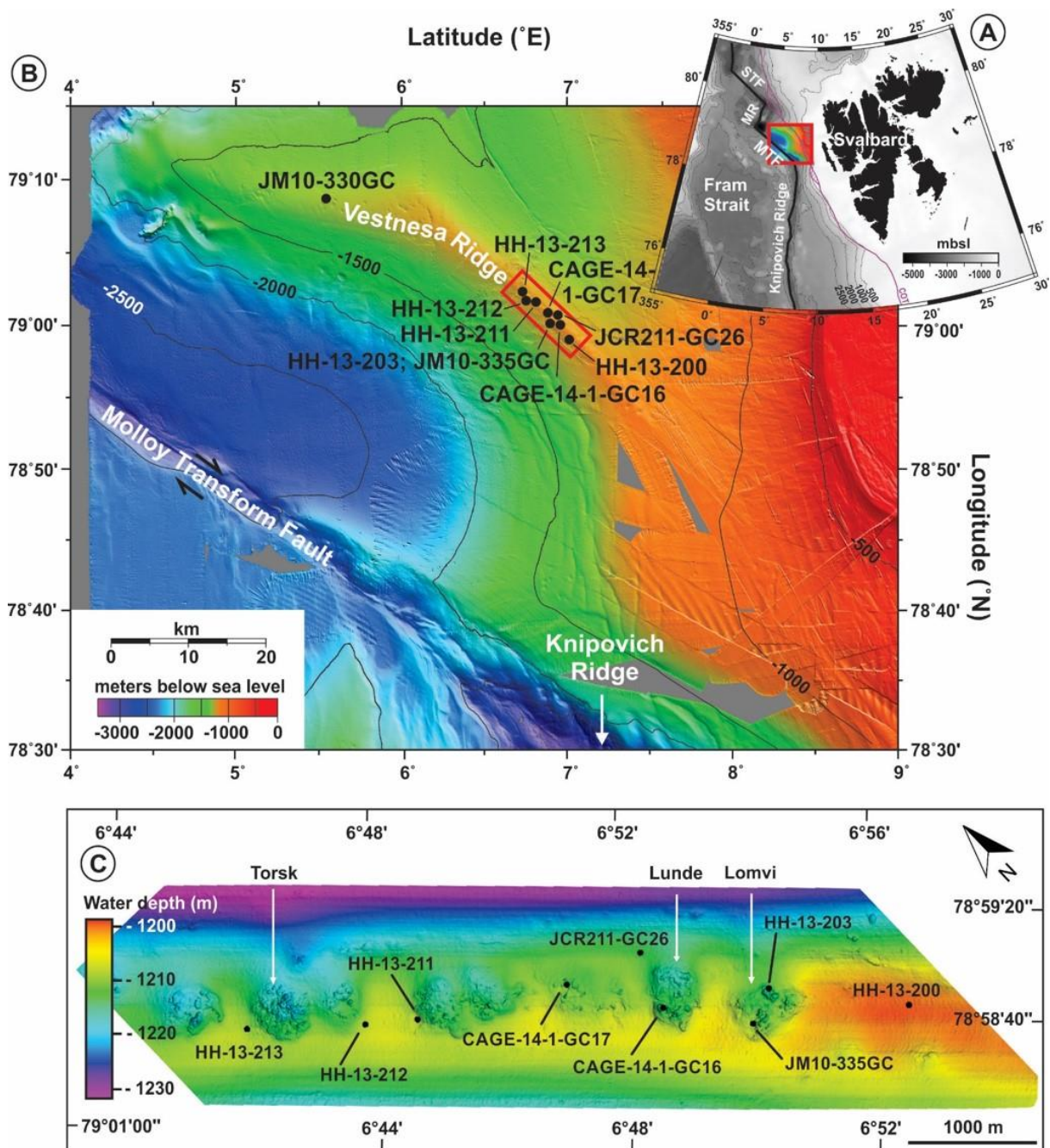
159 Seeps at Vestnesa Ridge produce up to 900 m high gas flares that probably emit a mixture of microbial
160 and thermogenic gas (Smith et al., 2014; Panieri et al., 2017b). A Bottom Simulating Reflector (BSR)
161 located ~160-180 m bsf (meters below seafloor) as well as an underlying zone of high amplitudes and
162 anomalously low seismic velocities indicate the presence of free gas at the base of the GHSZ (Petersen
163 et al., 2010; Goswami et al., 2015; Plaza-Faverola et al., 2015). Vertical fluid flow conduits (chimneys)
164 cross the BSR, intersect the overlying sediments, connect to the seafloor at pockmarks, and thus allow
165 vertical fluid migration (Petersen et al., 2010; Bünz et al., 2012). Circular seafloor depressions, known
166 as pockmarks, have a diameter of up to 700m, align along the crest of Vestnesa Ridge, and have a
167 complex topography with ridge-like structures and sub-depressions (pits) of ca. 50 m in diameter (Vogt
168 et al., 1994; Bünz et al., 2012; Panieri et al., 2017b; Fig. 1c). Seepage within the pockmarks Lunde and
169 Lomvi (Fig. 1c) is heterogeneous. The presence of bacterial mats and chemosynthetic tubeworms
170 suggest slow and pervasive (diffuse) fluid flow, while flares originating from pits (ca. 50m in diameter)
171 within the pockmarks and with sparse carbonate blocks at the seafloor may be evidence of strong
172 (focused) fluid flow (Panieri et al., 2017b). The pockmarks are actively releasing gases into the water
173 column in the south-eastern segment of Vestnesa Ridge but are inactive in the north-western segment
174 (Bünz et al., 2012; Smith et al., 2014; Plaza-Faverola et al., 2015). Several seepage episodes since the

175 onset of Northern Hemispheric glaciations, ca. 2.7 Ma ago, and within the last 17 cal ka have been
176 inferred from seismic interpretation of buried pockmarks and mounds within chimney structures and
177 foraminiferal stable carbon isotope records (Panieri et al., 2014; Consolaro et al., 2015; Plaza-Faverola
178 et al., 2015; Schneider et al., 2017; Szybor and Rasmussen 2017a). It has been suggested that an active
179 petroleum system was established offshore north-western Svalbard approximately 6 Ma ago when
180 hydrocarbon generation from deeply buried Miocene source rocks commenced (Knies et al. 2018).

181 Vestnesa Ridge is located between the western Svalbard continental margin and the ultra-slow
182 spreading Arctic ridge systems in the Fram Strait (Fig. 1a) (Talwani and Eldholm, 1977; Engen et al.,
183 2008; Johnson et al., 2015). It is bounded by the Spitsbergen Transform Fault and the ultraslow
184 spreading Molloy Ridge to the north, and the Molloy Transform Fault and the Knipovich Ridge to the
185 south (Crane et al., 2001; Vanneste et al., 2005; Winkelmann et al., 2008; Plaza-Faverola et al., 2015;
186 Johnson et al., 2015; Fig. 1a; b). Faulting and fracturing in response to tectonic stress variations over
187 the past 2.7 Ma is believed to exert an important control on seepage activity along the ridge (Plaza-
188 Faverola et al., 2015).

189 Two water masses dominate the present-day oceanographic setting of the Fram Strait: the West
190 Spitsbergen Current (WSC) and the East Greenland Current (EGC). The WSC, which is the northernmost
191 branch of the warm and saline Norwegian Atlantic Current, moves northwards along the western
192 Svalbard continental margin (Aagaard et al., 1987). It sustains ice-free conditions in the eastern Fram
193 Strait throughout most of the year and transports Atlantic water into the Arctic Ocean (Schauer et al.,
194 2004; Cokelet et al., 2008; Beszczynska-Möller et al., 2012; Rebesco et al., 2013). The EGC runs
195 southwards in the western Fram Strait and transports cold and less saline Polar Surface Water into the
196 Atlantic (Aagaard et al., 1987; Woodgate et al., 1995; Beszczynska-Möller et al., 2012).

197



198

199

200 **Fig. 1. (A)** IBCAO map of the western Svalbard margin and eastern Fram Strait (Jakobsson et al., 2012).

201 The red square indicates the location of B. The continent-ocean transition (COT) is delineated in purple.

202 STF – Spitsbergen Transform Fault. MR – Molloy Ridge. MTF – Molloy Transform Fault. **(B)**

203 Swath bathymetry map of Vestnesa Ridge with the location of the studied cores. The red square

204 indicates the location of (C). Modified from Hustoft et al. (2009). **(C)** Seafloor reflection map from high

205 resolution 3D seismic data (6x6 m bin size) showing the pockmark field on the south-eastern Vestnesa

206 Ridge segment and projection of the studied cores. Pockmark names Lunde, Lomvi, and Torsk in
207 accordance with Panieri et al. (2017b).

208

209 3 Methods

210 3.1 Core collection and description

211 In this study, we examine ten sediment gravity cores collected from Vestnesa Ridge between 2008 and
212 2014 (Table 1). Eight cores were retrieved from the south-eastern segment of Vestnesa Ridge that has
213 active pockmarks (Fig. 1b). Core HH-13-200 was recovered from the southernmost location 3.5 km
214 away from the nearest active pockmark (Lomvi). In contrast, sediment core JM10-330GC was taken
215 from an inactive pockmark at the north-western ridge segment. Reference core HH-13-212 was
216 collected from a site where modern and paleo-seepage evidence was absent. The coring transect
217 covers 35.8 km with distances between the cores varying from 0.1 to 27.7 km (Table 1). Selected results
218 from these cores have been published elsewhere (Table 1).

219 After recovery, the cores were cut into 100 cm sections, split longitudinally, and kept cool at 5°C. All
220 following sediment descriptions and analyses have been performed at UiT The Arctic University of
221 Norway in Tromsø. Magnetic susceptibility (MS) and bulk density (BD) were measured in 1 cm intervals
222 using a GeoTek Multi-Sensor Core Logger (MSCL). The cores were described visually, X-ray-scanned
223 (Geotek MSCL-XR 3.0), and photographed (Jai L-107CC 3 CCD RGB Line Scan Camera).

224 For reference core HH-13-212, ice-rafted debris (IRD, size > 2 mm) was counted using X-ray scans.
225 Geochemical data from selected cores (HH-13-200; -203; -211; -213) were acquired with an Avaatech
226 XRF Core Scanner at 1 cm steps using the following settings: down-core slit size 10 mm; cross-core slit
227 size 12 mm; 10 kV; 1000 µA; no filter; and 10 seconds measuring time per step; same settings but 50
228 kV and 20 seconds measuring time per step for barium. The raw data were subsequently processed
229 with the software WinAxil. For the purpose of this study, we report the strontium (Sr), calcium (Ca),
230 barium (Ba), and sulphur (S) counts normalised to either titanium (Ti) or to the sum of the eight most

231 common elements in our records (Sum8), which are silicon, strontium, potassium, calcium, zirconium,
 232 rubidium, titanium, and iron.

233

234 **Table 1.** Coring coordinates, year of recovery, sediment recovery, depth, distance between cores,
 235 and seafloor setting of the sediment gravity cores used in this study. Cores are listed from SE to NW.

236

Core ID	Coordinates	Year	Recovery (cm)	Depth (m bsf)	Distance to next core (km)	Seafloor setting	Reference and cruise
HH-13-200	78.981 °N 7.061 °E	2013	270	1205	3.70	Undisturbed seafloor	This study; Cruise CAGE-HH-2013
HH-13-203	79.002 °N 6.928 °E	2013	300	1210	0.1	Pockmark with flare (Lomvi)	Ambrose et al., 2015; Schneider et al., 2017; Cruise CAGE-HH-2013
JM10-335GC	79.002 °N 6.922 °E	2010	485	1197	0.7	Pockmark with flare (Lomvi)	Sztybor and Rasmussen 2017a; Cruise JM10
CAGE-14-1-GC16	79.008 °N 6.900 °E	2014	475	1217	0.46	Pockmark with flare (Lunde)	This study; Cruise CAGE 14-1
JCR211-GC26	79.011 °N 6.907 °E	2008	386	1210	0.60	Pockmark with flare	Panieri et al., 2014; Cruise JR211
CAGE-14-1-GC17	79.013 °N 6.880 °E	2014	440	1207	1.18	Pockmark	This study; Cruise CAGE 14-1
HH-13-211	79.018 °N 6.831 °E	2013	498	1202	0.40	Pockmark	Ambrose et al., 2015; Cruise CAGE-HH-2013
HH-13-212	79.020 °N 6.816 °E	2013	519	1202	0.91	Undisturbed seafloor	Reference core This study; Cruise CAGE-HH-2013
HH-13-213	79.025 °N 6.782 °E	2013	520	1203	27.76	Pockmark with flare (Torsk)	This study; Cruise CAGE-HH-2013
JM10-330GC	79.130 °N 5.600 °E	2010	420	1300		Pockmark	Consolaro et al., 2015; Cruise JM10

237

238

239 3.2 Chronology and age models

240 Stratigraphic correlation of the sediment cores is obtained through radiocarbon-dated MS records and
 241 associated tie points known from established stratigraphic marker horizons at the western Svalbard

242 continental margin (Table 2, Jessen et al., 2010; Szybor and Rasmussen, 2017a). All calibrated ages
 243 presented in the following text will be in calendar years before present (cal BP) A.D. 1950 with a
 244 standard deviation of 2σ .

245 Defined stratigraphic marker horizons include clast-rich laminated sediments (within the LGM; 24-23.5
 246 ka), fine-grained laminated sediments (Bølling interstadial; 14.7-14.3 ka), and a structureless layer rich
 247 in *Coscinodiscus* spp. diatoms (Early Holocene; 10.1-9.8 ka) that have been traced along the western
 248 Svalbard continental margin between 76 and 79°N by Jessen et al. (2010; Table 2). Both the
 249 structureless diatom-rich layer and the laminated sediments require microscopic examinations of the
 250 sediment or X-ray scanning for detection. The clast-rich laminated sediment can be identified as a dark
 251 sediment layer that is characterised by a sharp drop in MS, gradually increasing BD throughout the
 252 interval, and abundant IRD (Jessen et al., 2010).

253 Szybor and Rasmussen (2017a) proposed the correlation of the established stratigraphic marker
 254 horizons to the Vestnesa Ridge and provided additional radiocarbon ages. Some of the dates were
 255 performed on foraminiferal samples having low $\delta^{13}\text{C}$ that were clearly affected by diagenetic
 256 alteration. Radiocarbon dates obtained from such altered samples yield an older age due to exposure
 257 to methane-derived dissolved inorganic carbon and diagenetic alteration (Uchida et al., 2008). For this
 258 paper, we only use a selection of the ages obtained by Ambrose et al. (2015) and Szybor and
 259 Rasmussen (2017a) where $\delta^{13}\text{C}$ signature is characteristic of normal marine conditions.

260

261 **Table 2.** Stratigraphic tie points (TP) and marker horizons from the western Svalbard continental
 262 margin used for core correlation.

263

Interval	Min. Age cal years BP	Max. Age cal years BP	TP	Reference
Diatom-rich layer	9,840 ± 200	10,100 ± 150	2; 3	Jansen et al., 1983; Stabell, 1986; Jessen et al., 2010; Müller and Stein, 2014

Local MS max above laminated sediment interval	14,070 ± 210		4	Jessen et al., 2010
Laminated sediment interval	14,300 ± 260	14,780 ± 220	5; 6	Elverhøi et al., 1995; Birgel and Hass, 2004; Jessen et al., 2010; Lucchi et al., 2015
Event 1	23,550 ± 185	24,080 ± 150	7; 8	Knies and Stein, 1998; Vogt et al., 2001; Jessen et al., 2010
Nearest local MS min below Event 1	27,500 ± 270		9	Jessen et al., 2010

264

265

266 We have further improved the stratigraphic control with one additional ¹⁴C AMS radiocarbon age. The
 267 additional radiocarbon dating was carried out at the Beta Analytic Radiocarbon Dating facilities in
 268 Miami, US. A conventional radiocarbon age of 28,090 +/- 150 years was obtained from a basal sample
 269 of core HH-13-213 (455 cm, laboratory code Beta-456619). The age was converted into calendar years
 270 using the calibration program Calib 7.1 (Stuiver et al., 2014) with a marine reservoir age of -400 years
 271 that was incorporated within the Marine13 calibration curve (Reimer et al., 2013). In addition, a
 272 regional reservoir age correction ΔR of 7 ± 11 was applied (Mangerud et al., 2006). The age model is
 273 based on the calibrated ages obtained from the peaks of the probability curves within the 2σ range.
 274 The calibrated result was an age of 29,490 +/- 287 years BP. Based on the stratigraphic tie points (Table
 275 2) and the additional radiocarbon age, we calculate linear sedimentation rates for the stratigraphic
 276 marker horizons and the intermediate sediment intervals (supplementary material S1).

277

278 3.3 Stable isotope analyses of foraminifera

279 Samples for stable isotope analysis of foraminiferal calcite tests were typically collected at 10 cm
 280 intervals and at 5 cm intervals from the reference core HH-13-212 (Table S2). Samples from cores HH-
 281 13-203 (depth interval from 220 to 270 cm) and HH-13-211 (depth interval from 390 to 470 cm) were
 282 obtained at higher spatial resolution (Table S2). The samples were wet-weighed, freeze-dried, dry-
 283 weighted, and wet-sieved (mesh sizes 63 μm, 100 μm, 1 mm). The sieve residues were dried at 40°C

284 and subsequently investigated using optical microscopes. Benthic (*Cassidulina neoteretis*
285 [Seidenkrantz, 1995]; *Melonis barleeanus* [Williamson, 1858]) and planktic foraminifera
286 (*Neogloboquadrina pachyderma* sinistral (sin) [Ehrenberg, 1861]) were picked for isotope
287 measurements from the dry residue of the > 100 µm size fraction. Those species were selected since
288 they are abundant throughout the cores, and common in the Arctic Ocean (Wollenburg and
289 Mackensen 1998; Wollenburg et al., 2001; Zamelczyk et al., 2012). The same foraminiferal species have
290 been used in similar studies from Vestnesa Ridge (Table 1).

291 Stable oxygen ($\delta^{18}\text{O}$) and carbon ($\delta^{13}\text{C}$) isotope analyses of foraminiferal tests were performed using a
292 ThermoFinnigan MAT252 mass spectrometer coupled to a CarboKiel-II carbonate preparation device
293 at the Serveis Científico-Técnicos of the University in Barcelona in Spain. Each sample of *Cassidulina*
294 *neoteretis* (236 samples), *M. barleeanus* (18 samples), *N. pachyderma* sin (172 samples) consists of 15
295 to 30 tests. Analytical precision was estimated to be better than $\pm 0.08\text{‰}$ for oxygen and $\pm 0.03\text{‰}$ for
296 carbon by measuring the certified standard NBS-19. We report all isotope results in standard delta
297 notation relative to Vienna Pee Dee Belemnite (VPDB). For already published stable isotope records
298 that are included in this study, details for sample preparation and stable isotope measurements can
299 be found in the references given in Table 1.

300

301 3.4 MDAC analyses – stable isotopes and mineralogy

302 Stable oxygen and carbon isotope analyses of 37 authigenic carbonate nodules from different cores
303 were performed using a ThermoScientific MAT253 mass spectrometer coupled to a Finnigan Gasbench
304 II at the Stable Isotope Laboratory at UiT The Arctic University of Norway in Tromsø. Analytical
305 precision was estimated to be better than $\pm 0.07\text{‰}$ VPDB.

306 Where enough material was present, we performed XRD analyses of unoriented carbonate samples
307 using a Bruker D8 Advance X-ray diffractometer (Cu K_{α} radiation in 3-75° 2 θ range) at the Geological
308 Survey of Norway in Trondheim. The quantitative mineralogical composition of the carbonate phases
309 was interpreted and modelled by using the Rietveld algorithm-based code Topas-4 by Bruker.

310 Following a displacement correction of the spectrum made on the main quartz peak, the displacement
311 of calcite d_{104} was used to estimate the amount of $MgCO_3$ mol % (Goldsmith and Graf, 1958).

312

313 4 Results and Discussion

314 4.1 Lithology, chronology and core correlation

315 The length of the ten investigated sediment cores varies between 2.7 and 5.2 m with an approximate
316 age range from 31.9 ka BP (pre-LGM) to 10 ka BP (Early Holocene). The sedimentological description
317 and the chronological framework of already published cores can be found in the references given in
318 Table 1.

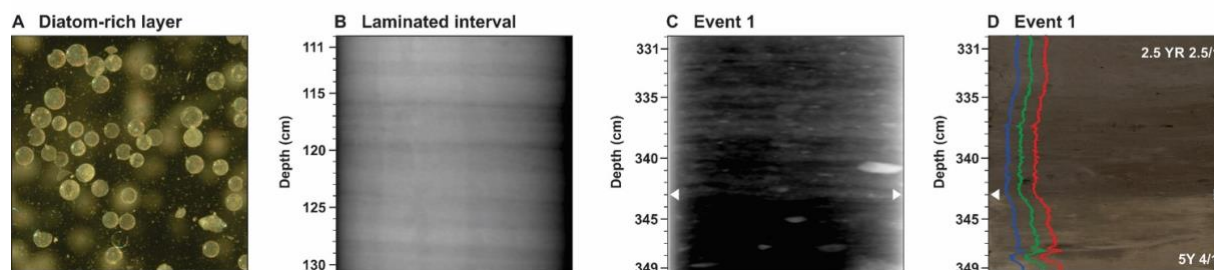
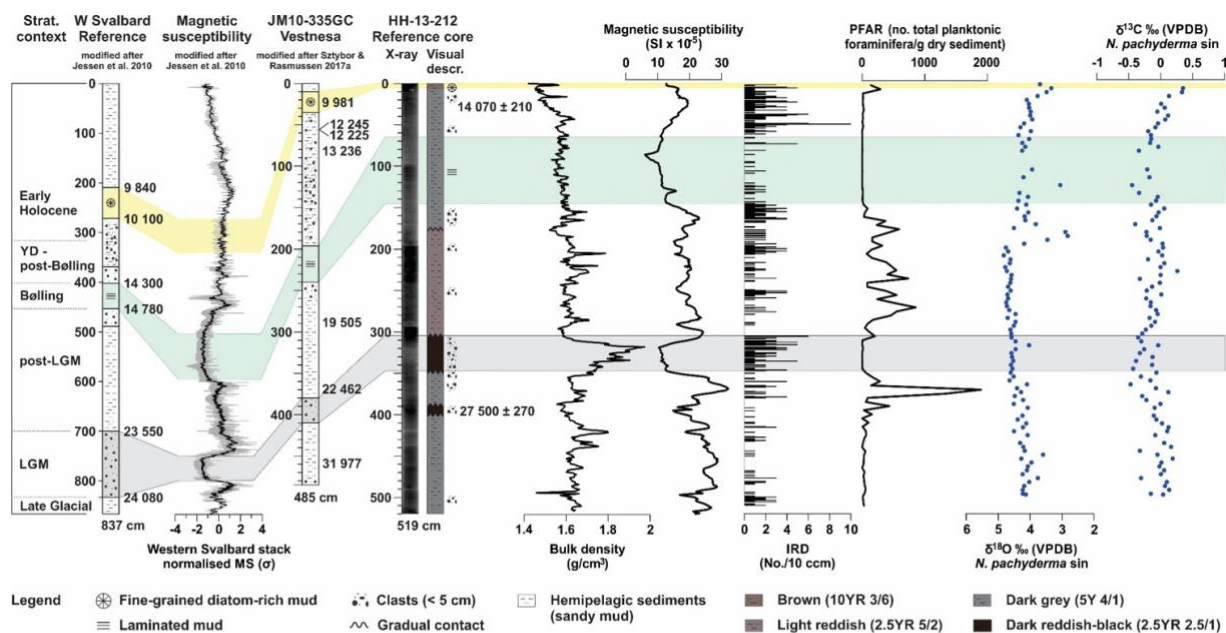
319

320 4.1.1 Reference core HH-13-212 and regional correlations

321 The 519 cm long reference core HH-13-212 was collected outside pockmarks on the crest of Vestnesa
322 Ridge where methane seepage is absent. The core is composed of silty clay with intervals rich in IRD
323 and includes all three main stratigraphic marker horizons for the western Svalbard continental margin
324 spanning from the LGM to the Early Holocene (Tab. 3; Fig. 2). The diatom-rich interval occurs in the
325 top 5 cm of the core (max. age 10.1 ka BP; Early Holocene), laminated sediments occur between 65 cm
326 (14.3 ka BP) and 155 cm (14.7 ka BP; Bølling), and dark laminated coarser sediment occurs at 309-353
327 cm (24-23.5 ka BP; within the LGM; Tab. 3; Fig. 2). This interval is known as “Event 1” (Knies and Stein,
328 1998) and is dated to approximately 23-19.4 ^{14}C ka BP (Elverhoi, 1995; Andersen et al., 1996; Vogt et
329 al., 2001) or 24 ka BP (^{14}C age: $20,040 \pm 325$; lab code KIA365, Knies and Stein, 1998).

330 The MS values largely follow the western Svalbard MS stack curve (Jessen et al., 2010, Fig. 2). For the
331 description of the lithology and foraminifera content of core HH-13-212, the main stratigraphic marker
332 horizons, and major paleoceanographic and environmental changes the reader is referred to the data
333 in brief article.

334



335

336

337 **Fig. 2.** Lithology and magnetic susceptibility (MS) of the western Svalbard reference record obtained
 338 by Jessen et al. (2010). Lithology of core JM10-335GC modified after Szybor and Rasmussen (2017a).
 339 X-ray image, lithology, BD, MS, IRD content, PFAR (planktic foraminiferal accumulation rate), stable
 340 oxygen and carbon isotope records from *N. pachyderma* sin from Vestnesa Ridge reference core HH-
 341 13-212. LGM – Last Glacial Maximum. HE 1 – Heinrich Event 1. YD – Younger Dryas. The negative MS
 342 peaks at 100 and 500 cm are artefacts due to change in core section. **(A)** Diatom-rich interval.
 343 Photograph of the > 63 μm fraction from microscope, magnification is 16x. HH-13-212, 5 cm bsf. **(B)**
 344 Laminated interval. X-ray scan of fine-grained laminated sediments. HH-13-212, 110-131 cm bsf. **(C)**
 345 Event 1 sediments. X-ray scan of fine-grained laminated sediment providing a matrix for abundant
 346 gravel sized clasts. HH-13-212, 330-350 cm bsf. **(D)** Event 1 sediments. Colour scan, RGB colour values,
 347 and lower contact of the Event 1 interval. HH-13-212, 330-350 cm bsf. An arrow in panels C and D
 348 marks the base of the Event 1 sediments.

349

350 4.1.2 Cores from active and inactive pockmarks on Vestnesa Ridge

351 The eight sediment cores recovered from active or inactive pockmarks, and the southernmost core
352 HH-13-200, consist of dark grey silty clay of late Pleistocene and Early Holocene age with layers rich in
353 IRD and shell fragments (Fig. 3).

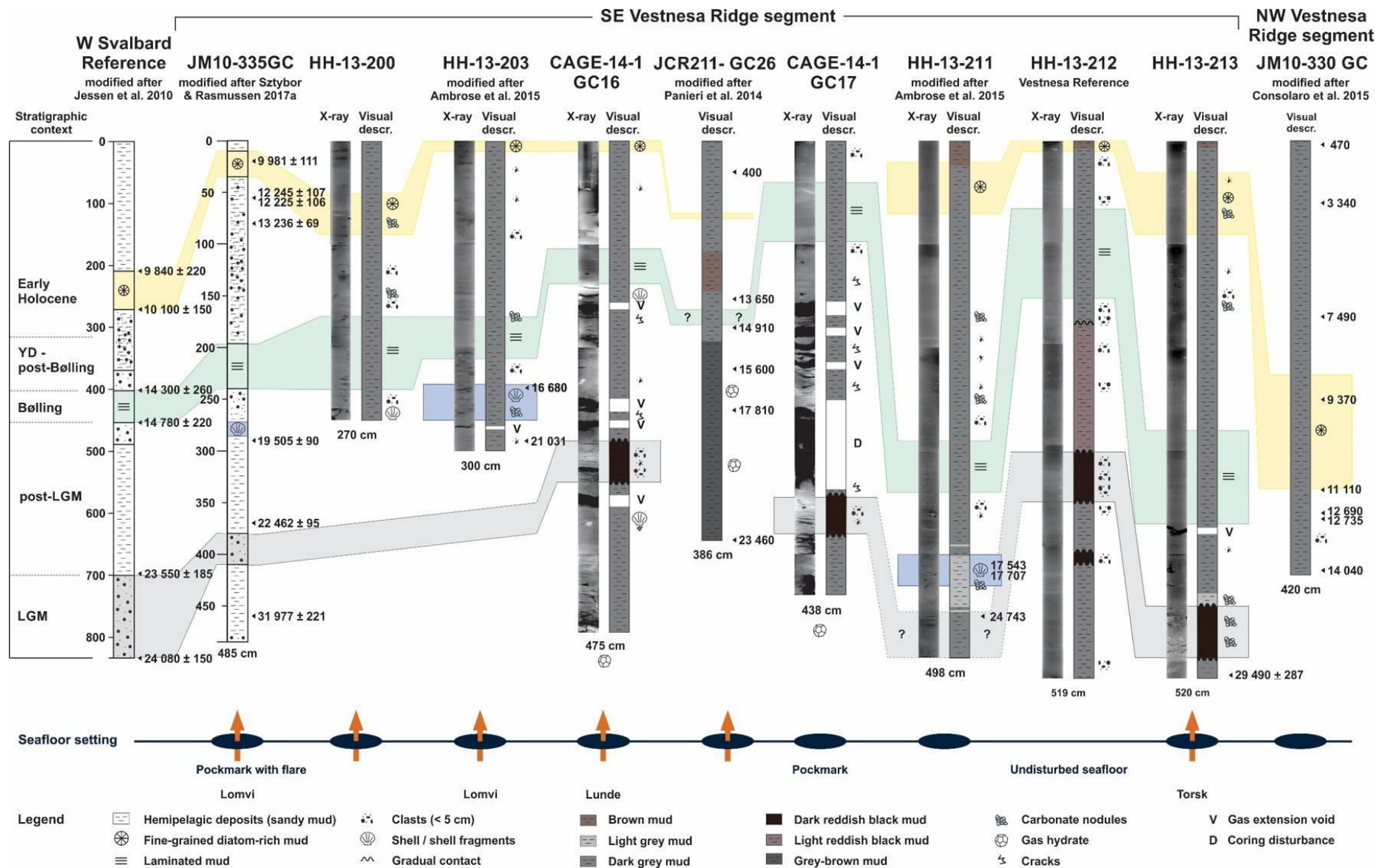
354 Magnetic susceptibility signals are typically low (Table 4). This is common in methane seeps where
355 iron-oxides such as ferromagnetic magnetite (Fe_3O_4) are exposed to hydrogen-sulphide produced by
356 AOM, experience reduction to paramagnetic pyrite (FeS_2), and cause significant reduction or loss of
357 the MS signal (Canfield and Berner, 1987; Riedinger et al., 2005; März et al., 2008; Dewangan et al.,
358 2013). Nevertheless, all three typical stratigraphic marker horizons can be recognised in most of the
359 sediment cores and allow core correlation (Table 3). The 25-50 cm thick Event 1 sediments were
360 identified based on X-ray images and a reddish-black layer (Munsell colour: 2.5YR 2.5/1) in cores CAGE-
361 14-1-GC16; CAGE-14-1-GC17; HH-13-211, and HH-13-213. A radiocarbon date of 24,743 years BP at
362 460.5 cm obtained from planktic foraminifera confirms the upper boundary of Event 1 (Ambrose et al.,
363 2015). The total thickness of the laminated interval varies between 30 cm and 90 cm. In most cores,
364 the interval rich in *Coscinodiscus* spp. diatoms occurs at or near the core top, indicating Early Holocene-
365 aged sediments near the seafloor. The calculated linear sedimentation rates reveal rapid
366 sedimentation during the LGM (75-90 cm ka^{-1}) and the Early Holocene (67-188 cm ka^{-1} ; supplementary
367 material S1).

368 Interestingly, sediment cores from the western Svalbard continental shelf and slope, including the
369 south-eastern Vestnesa Ridge segment, share the absence of Early Holocene sediments (Elverhøi et
370 al., 1995; Howe et al., 2008; Szybor and Rasmussen 2017a; 2017b), presumably due to the erosive
371 force of the WSC resulting in non-deposition or sediment removal. Mooring studies across the Fram
372 Strait reveal the present-day WSC has two branches with a narrow and strong core shallower than
373 1000 m and maximum northwards velocities of 20 cm s^{-1} , and an offshore branch below 1400 m with
374 northwards velocities of 5-10 cm s^{-1} (Beszczynska-Möller et al., 2012; Rebesco et al. 2013). The strong

375 WSC core may have winnowed unconsolidated fine-grained sediments from the easternmost part of
376 Vestnesa Ridge, explaining the narrow and sharp bathymetric expression of the ridge along its eastern
377 segment (Fig. 1). In contrast, the north-western ridge segment, located in 1300 m water depth, has a
378 more widespread and gently rounded geometry. It may have experienced less strong current velocities
379 and therefore retained Holocene sediments.

380

381



383 **Fig. 3.** Core description and correlation with published records from Vestnesa Ridge and the western
 384 Svalbard margin. Note the different depth scale on the W Svalbard reference record. The depth of the
 385 laminated sediments in core JCR211-GC26 was estimated assuming linear sedimentation between the
 386 ages obtained by Panieri et al. (2014). Pockmark names according to Panieri et al. (2017b). LGM – Last
 387 Glacial Maximum. HE 1 – Heinrich Event 1. YD – Younger Dryas.

388

389

390

391

392 **Table 3.** Depth intervals of the main sedimentary units and fossil content, given in cm below seafloor
 393 (bsf). *The depth of the laminated sediments in core JCR211-GC26 was estimated assuming linear
 394 sedimentation between the ages obtained by Panieri et al. (2014). bsf - below sea floor.

395

Core ID	Diatom-rich sediments	Laminated sediments	Shell bed interval	Event 1 sediments
	cm bsf	cm bsf	cm bsf	cm bsf
HH-13-200	50-90	170-240	-	-
HH-13-203	0-10	172-210	236-268	-
JM10-335GC	10-35	200-240	278	380-410
CAGE-14-1-GC16	0-10	105-137	-	290-330
JCR211-GC26	117-120	167-178*	-	-
CAGE-14-1-GC17	-	40-98	-	347-372
HH-13-211	20-70	287-340	400-430	? (> 465)
HH-13-212	0-5	65-155	-	309-343
HH-13-213	30-90	280-370	-	450-498
JM10-330 GC	225-335	-	-	-
Time Period	Early Holocene	Bølling interstadial	HE 1	LGM
Age (cal years BP)	10,080-9,840	14,780-14,300	17,707-16,680	23,550-24,080

Interpretation	Northward movement of the Oceanographic Polar Front	Deglacial plumite from rapid SBIS disintegration	Seafloor methane seepage	SBIS maximum extent during LGM
Reference	Jansen et al., 1983; Stabell, 1986; Jessen et al., 2010; Müller and Stein, 2014	Elverhøi et al., 1995; Birgel and Hass, 2004; Jessen et al., 2010; Lucchi et al., 2015	Bond et al., 1992; Hemming, 2004; Ambrose et al., 2016; Stzybor and Rasmussen, 2017a	Knies and Stein, 1998; Vogt et al., 2001; Jessen et al., 2010

396

397

398 In the recovered sediments, the following features were caused by the presence of methane and AOM.

399 Firstly, the cores retrieved from pockmarks with active flares had a strong odour of hydrogen-sulphide

400 (H₂S). Secondly, based on the porewater profiles, the present-day SMTZ is shallow in cores HH-13-200

401 (75-110 cm bsf), HH-13-203 (100-140 cm bsf) and JCR211-GC26 (70-120 cm bsf) as revealed by

402 porewater profiles (Hong et al., 2016, Table 4), these intervals have estimated depositional ages

403 between 13.4 ka and 4.8 ka, respectively (Table 4). Thirdly, near-surface gas hydrate was recovered in

404 cores CAGE-14-1-GC16 (in core catcher), CAGE-14-1-GC17 (in core catcher), and JCR211-GC26 (hydrate

405 bearing sediment at 200-380 cm, Fig. 3). Fourthly, irregularities such as cm-scale voids and cracks in

406 cores where gas hydrate was recovered are likely to be introduced by gas expansion during core

407 recovery. Finally, carbonate nodules occur in cores HH-13-203 (220-280 cm), HH-13-211 (470-498 cm),

408 and in core HH-13-213 below 450 cm bsf (Fig. 3). Additional mm-sized micritic carbonates were found

409 throughout the cores listed above, and in HH-13-200 when examining the > 100µm fraction for

410 foraminiferal studies.

411

412

413 **Table 4.** Depth of the SMTZ in the studied cores, host sediment age, and description of magnetic

414 susceptibility data (MS). Host-sediment age at the SMTZ position was calculated from linear

415 sedimentation rates (S1). Porewater profiles from Hong et al. 2016. * Ambrose et al. 2015.

416

417

418

419

420

421

422

423

424

425

426

427

428

429

430

431

432

433

434

435

436

437

Core ID	Present-day SMTZ (cm bsf)	Host sediment age at SMTZ position (cal ka BP)	MS
HH-13-200	75-115 (porewater profile available)	11.4 – 10	Depleted
HH-13-203	100-140 (porewater profile available)	13.4 – 12.4	Depleted*
JM10-335GC	–	–	Depleted
CAGE-14-1-GC-16	–	–	Depleted
JCR211-GC26	70-120 (porewater profile available)	10.1 – 4.8	no data
CAGE-14-1-GC-17	–	–	Depleted
HH-13-211	165-225 (inferred)	13.1 – 11.9	Depleted*
HH-13-212	–	–	Normal
HH-13-213	70-100 (inferred)	10.3 – 10	Depleted
JM10-330 GC	–	–	Normal
Time frame	recent	13.4 – 4.8	
	(cal years BP)		
Interpretation	SO ₄ ²⁻ -CH ₄ interface, occurrence of SO ₄ ²⁻ - dependent AOM	SMTZ in ancient host sediments	AOM-related exposure to H ₂ S

438 Complete valves and shell fragments of juvenile and mature bivalves and gastropods in cores HH-13-
439 203 and HH-13-211 (Fig. 3) represent a chemosynthetic bivalve community (hereafter named “shell
440 bed”) that was first described in Ambrose et al. (2015). *Vesicomysidae* bivalves dominate the species
441 assemblage (Hansen et al., 2017). Some bivalves and ostracods were found with articulated valves,
442 indicating they likely died *in-situ*. Ambrose et al. (2015) dated the shell bed to 16,7 to 17,7 ka BP using
443 planktic foraminifera and bivalves without MDAC overgrowth and $\delta^{13}\text{C}$ values higher than -1.6‰ that
444 suggest valid ages.

445

446 4.2 Stable isotope records

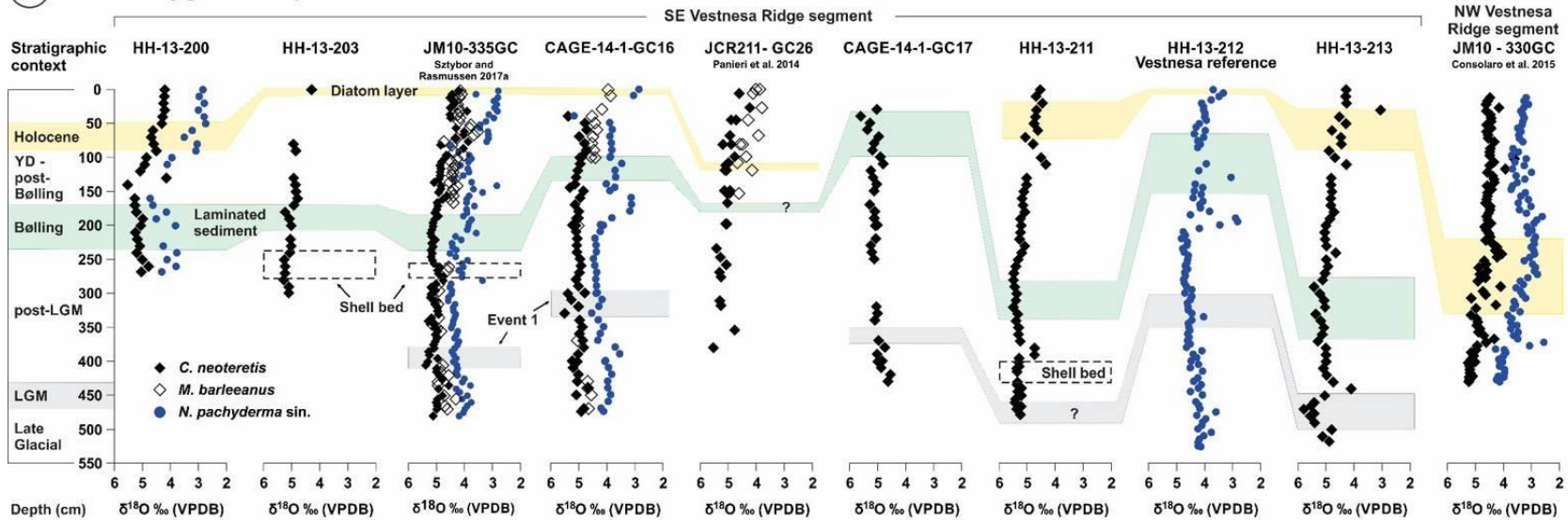
447 4.2.1 Oxygen isotopes

448 Our records are consistent with the $\delta^{18}\text{O}$ stratigraphy for planktic foraminifera from the western
449 Svalbard margin (e.g. Elverhøi et al., 1995; Nørgaard-Pedersen et al., 2003; Rasmussen et al., 2007),
450 the Yermak Plateau (Nørgaard-Pedersen et al., 2003) and the northern Barents Sea margin (Knies et
451 al., 1999; 2000) during the LGM, post-LGM, and Early Holocene.

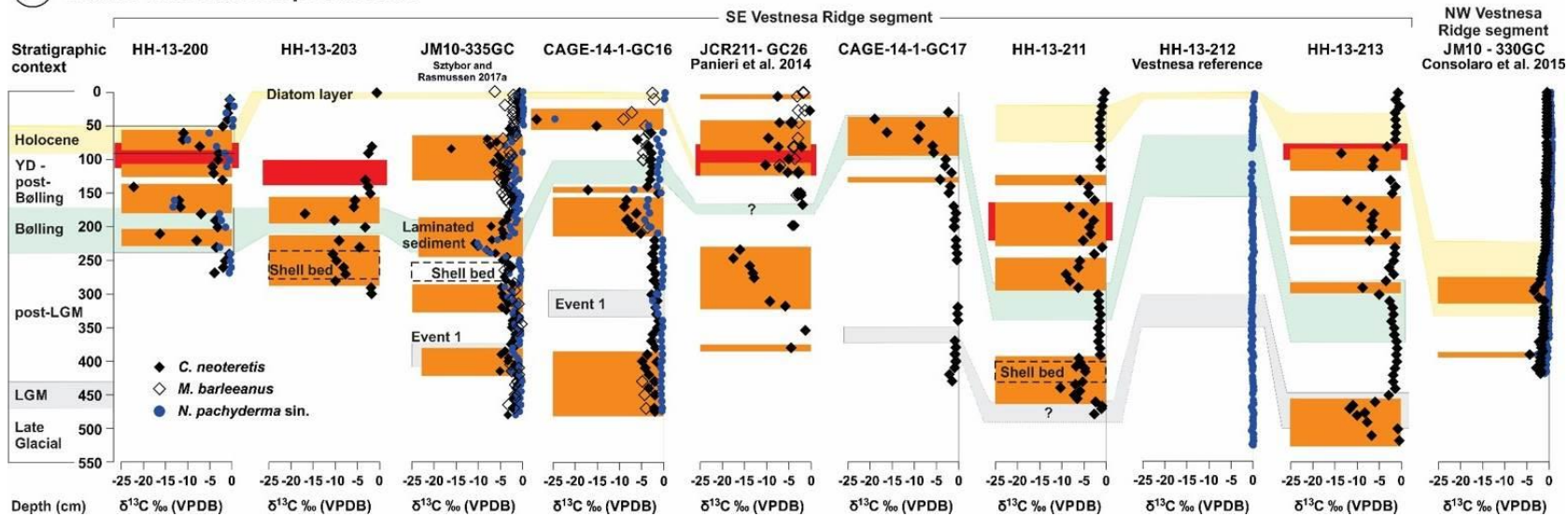
452 The $\delta^{18}\text{O}$ values from planktic foraminifera during the LGM in the Fram Strait are typically around 4.5
453 to 4.8‰ (e.g. Hebbeln et al., 1994; Elverhøi et al., 1995; Nørgaard-Pedersen et al., 2003). We obtain
454 similar values during the LGM (Figs. 2a and 4a; CAGE-14-1-GC16; HH-13-212). Termination 1 (17.8-16.7
455 ka BP) is defined by low $\delta^{18}\text{O}$ values indicative of melt-water contributions from the SBIS and can be
456 recognised in the entire Polar North Atlantic (Hebbeln et al., 1994; Elverhøi et al., 1995; Nørgaard-
457 Pedersen et al., 2003).

458 At Vestnesa Ridge, values as low as 2.8-3‰ in *N. pachyderma* sin occur in post-LGM-aged sediments
459 (Figs. 2a and 4a, HH-13-212; CAGE-14-1-GC16). We suggest the $\delta^{18}\text{O}$ spike in the post-LGM sediments
460 marks Termination 1. During the Early Holocene, $\delta^{18}\text{O}$ values generally decrease. An additional, less
461 pronounced $\delta^{18}\text{O}$ spike in the Younger Dryas (Figs. 2a and 4a; HH-13-212; CAGE-14-1-GC16), signals
462 the beginning of interglacial conditions when northwards protruding warm Atlantic water masses
463 destabilised the ice tongues of tidewater glaciers and may have caused local meltwater pulses in the
464 northern North Atlantic (Elverhøi et al., 1995; Rasmussen et al., 2007; Slubowska-Woldengen et al.

A Stable oxygen isotope records



B Stable carbon isotope records



469 **Fig. 4.** $\delta^{18}\text{O}$ (A) and $\delta^{13}\text{C}$ (B) records of benthic (*C. neoteretis*; *M. barleeanus*) and planktic (*N.*
470 *pachyderma* sin) foraminifera. The Early Holocene diatom layer (9.8-10.1 ka BP), the laminated
471 sediment deposited during the Bølling interstadial (14.3-14.8 ka BP), and near the LGM (23.5-24 ka BP)
472 are indicated. LGM – Last Glacial Maximum. HE 1 – Heinrich Event 1. YD – Younger Dryas. Orange zones
473 are indicating the episodes of negative carbon excursions. See supplementary material S2 for the
474 foraminiferal $\delta^{13}\text{C}$ and $\delta^{18}\text{O}$ values. Red boxes indicate the position of the present-day SMTZ according
475 to table 4.

476

477 4.2.2 Carbon isotopes

478 The $\delta^{13}\text{C}$ record of planktic *N. pachyderma* sin from core HH-13-212 (Figs. 2; 4b) ranges between 0 and
479 -1‰ and can be considered as representative of normal marine conditions, expressed as $\delta^{13}\text{C}$ values
480 between $-0,5$ and $0,5\text{‰}$ (Knies and Stein, 1998). A $\delta^{13}\text{C}$ range between 0 and -1‰ is considered
481 representative of normal marine conditions in benthic *C. neoteretis* tests from the northern Barents
482 Sea (0 to -1‰ , Wollenburg et al., 2001) and a control site from the Håkon Mosby Mud Volcano ($-$
483 $1,15\text{‰}$, Mackensen et al., 2006). For *M. barleeanus*, McCorkle et al. (1990) observed $\delta^{13}\text{C}$ values of $-$
484 2‰ in the Atlantic Ocean.

485 In contrast, the majority of the $\delta^{13}\text{C}$ records of benthic and planktic foraminifera show between two
486 and five negative $\delta^{13}\text{C}$ excursions with amplitudes up to -29‰ (Fig. 4b). Negative $\delta^{13}\text{C}$ excursions in
487 benthic foraminifera occur in LGM sediments (HH-13-211; -213 ; JM10-335GC), during HE 1 (HH-13-
488 203; -211), during and after the Bølling interstadial (HH-13-200; -203 ; JM10-335GC; CAGE-14-1-GC16;
489 CAGE-14-1-GC17; HH-13-211; -213), and during the Early Holocene (HH-13-200; JCR211-GC26). In
490 some intervals, negative $\delta^{13}\text{C}$ excursions co-occur in benthic and planktic foraminifera (HH-13-200,
491 $60,5$ - $220,5$ cm; CAGE-14-1-GC16, $144,5$ - $209,5$ cm), while in others exclusively benthic foraminifera are
492 ^{13}C depleted (CAGE-14-1-GC16, $359,5$ - $439,5$ cm; JM10-330GC, 255 - 305 cm).

493 Living foraminifera can incorporate ^{13}C -depleted, methane-derived dissolved inorganic carbon (DIC)
494 while metabolically active, and/or likely ingest ^{13}C -depleted methanotrophic microbes, leading to

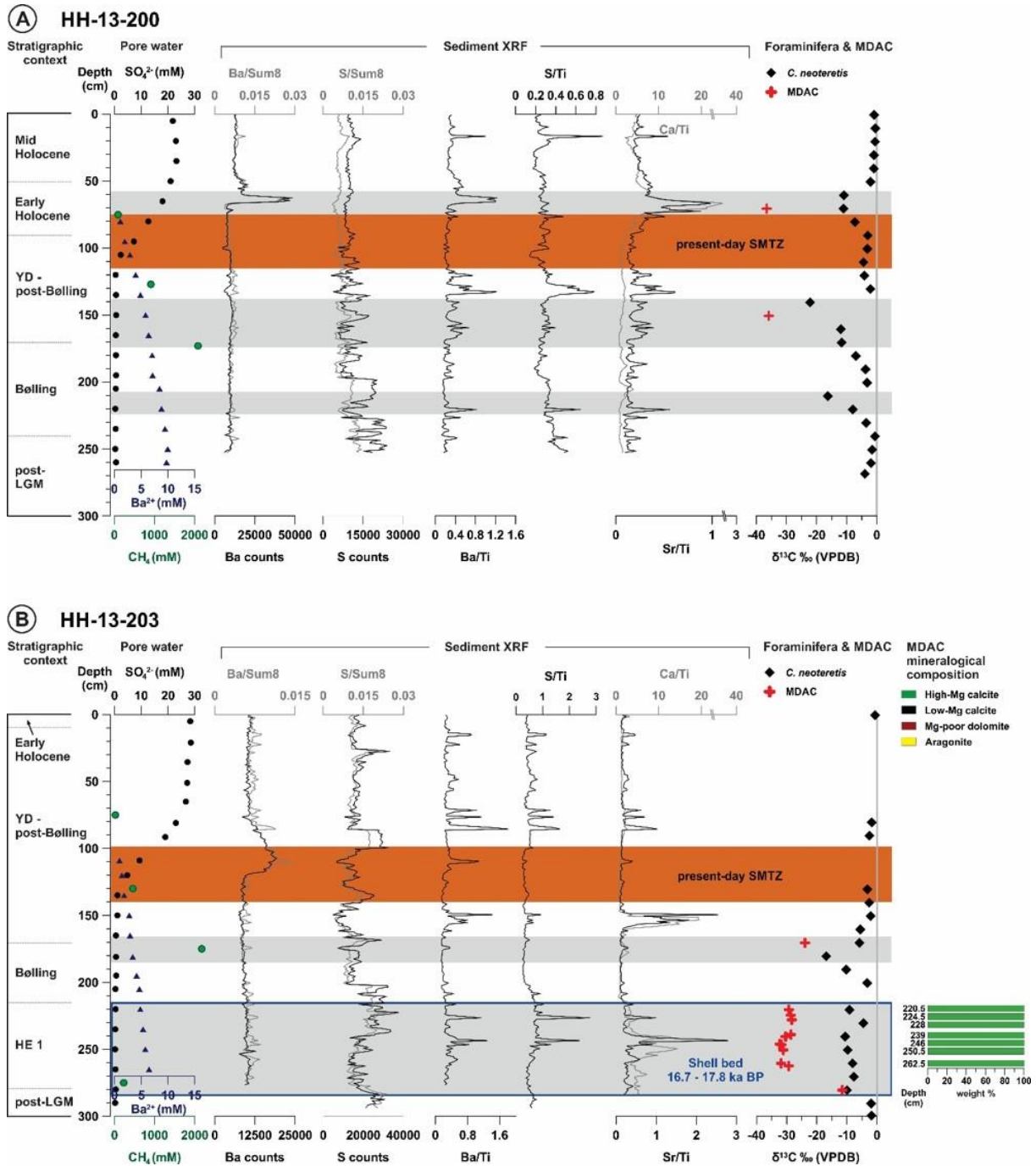
495 slightly negative $\delta^{13}\text{C}$ values as low as -5.6‰ (Rathburn et al., 2003; Hill et al., 2004; Panieri et al., 2006;
496 Panieri and Sen Gupta, 2008). However, values as low as -15‰, as we record in planktic foraminifera,
497 and -29‰ in benthic foraminifera, cannot be explained solely by metabolic activity of the foraminifera
498 in the presence of methane-derived DIC or foraminiferal diet. Furthermore, planktic foraminifera living
499 in the surface water are unlikely to encounter AOM-derived DIC as benthic organisms consume most
500 of the methane (Damm et al., 2005; Niemann et al., 2006; Reeburgh, 2007; Boetius and Wenzhöfer,
501 2013; Steinle et al., 2015). The strongly negative $\delta^{13}\text{C}$ signatures are most likely introduced after the
502 death of the foraminifera and burial of their tests in the sediment through the diagenetic alteration at
503 the SMTZ. Panieri et al. (2017a) investigated the boundaries between biogenic test calcite and
504 diagenetic overgrowth and showed that foraminiferal tests act as nucleation templates for MDAC.
505 Schneider et al. (2017) described the visual and geochemical characteristics of foraminiferal tests
506 experiencing diagenetic alteration during methane seepage. Such MDAC precipitation at the SMTZ
507 cumulatively adds a second phase of ^{13}C -depleted carbon on foraminiferal tests and causes negative
508 $\delta^{13}\text{C}$ values in the range of -7 to -36‰ (Torres et al., 2003b; Hill et al., 2004; Millo et al., 2005; Panieri
509 et al., 2009; Martin et al., 2010; Panieri et al., 2017a; Szybor and Rasmussen, 2017a; 2017b; Schneider
510 et al., 2017). We follow this interpretation and suggest that each negative $\delta^{13}\text{C}$ excursion is caused by
511 diagenetic alteration of the primary tests under the conditions of a relatively stable SMTZ at/close to
512 the seafloor due to enhanced methane flux.

513 Exclusively in the reference core HH-13-212, which is located close to active pockmarks, evidence for
514 methane seepage and MDAC precipitation is entirely absent in planktic foraminiferal $\delta^{13}\text{C}$ records (Figs.
515 2, 4b). Cores from pockmarks at the south-eastern ridge segment have the largest variability and
516 amplitudes in $\delta^{13}\text{C}$ while the north-western most core, JM10-330 GC, only shows two negative $\delta^{13}\text{C}$
517 excursions of comparably small amplitude (Fig. 4b). The easternmost core, HH-13-200, surprisingly
518 shows negative $\delta^{13}\text{C}$ excursions even though the core was recovered 3.5 km away from the nearest
519 active pockmark (Lomvi). This may be explained by the proximity of the core-site to non-outcropping
520 fluid flow related features, as observed in seismic data (A. Plaza-Faverola, unpublished data).

521

522 4.3 SMTZ migration in Holocene sediments

523 Negative foraminiferal $\delta^{13}\text{C}$ excursions are typically associated with elevated sediment Ca/Ti and Sr/Ti
524 elemental ratios and with the presence of carbonate-cemented nodules in cores HH-13-200; -203; -
525 211; and -213 (Figs. 5; 6). Elevated Ca/Ti elemental ratios identify sediment intervals with high Ca-
526 carbonate content, which can represent biogenic debris, such as foraminiferal tests or shells, or
527 inorganic MDAC precipitates. Peaks in Ca/Ti near the base of cores HH-13-203 (Fig. 5b) and HH-13-211
528 (Fig. 6a) are caused by bivalves and gastropods of the shell bed as described by Ambrose et al. (2015).
529 Large carbonate clasts in core HH-13-213 prevented XRF measurements deeper than 450 cm (Fig. 6b),
530 but an initial rise in Sr and Ca content is indicative of elevated carbonate content towards the base of
531 the core. Elevated Sr values are typical for aragonite, a common constituent of MDAC (Kastner et al.,
532 1990) that typically precipitates when the SMTZ is close to the sediment-water interface. The $\delta^{13}\text{C}$
533 values of the carbonate nodules range between -36.58‰ and -8.59‰ (supplementary material S3).
534 Our XRD analyses (supplementary material S4) indicate that high-Mg calcite (5-20mol% MgCO_3 , Burton
535 1993) dominates the carbonate phase in the nodules from HH-13-203 (Fig. 5b). High-Mg-calcite and
536 aragonite comprise the carbonate phase in the nodules from HH-13-213 (Fig. 6b). In HH-13-211
537 additional small fractions of low-Mg calcite ($< 5\text{mol}\% \text{MgCO}_3$, Burton 1993) and Mg-poor dolomite are
538 present (Fig. 6a). An earlier study of the shell bed host sediments in core HH-13-203 reveals the
539 presence of pyrite-encrusted tube-like features, framboidal pyrite, and botryoidal aggregates of
540 acicular aragonite crystals (Ambrose et al., 2015), as well as carbonate nodules, composed of
541 irregularly shaped 5-10 μm sized carbonate crystals cementing disseminated pyrite and detrital grains
542 (Schneider et al., 2017). Their $\delta^{13}\text{C}$ signatures, mineral composition, and the co-occurrence with
543 chemosynthetic bivalves suggest the carbonates are methane-derived and formed when the SMTZ was
544 located at the seafloor (Aloisi et al., 2000; Bohrmann et al., 2001; Greinert et al., 2001; Naehr et al.,
545 2007; Ambrose et al., 2015). We hence regard sediment records of MDAC, negative foraminiferal $\delta^{13}\text{C}$
546 excursions, and elevated Ca/Ti and Sr/Ti elemental ratios as indicators of multiple (past) SMTZ
547 positions and shallow subseafloor diagenesis due to methane cycling (grey bars in Figs. 5; 6).



549

550

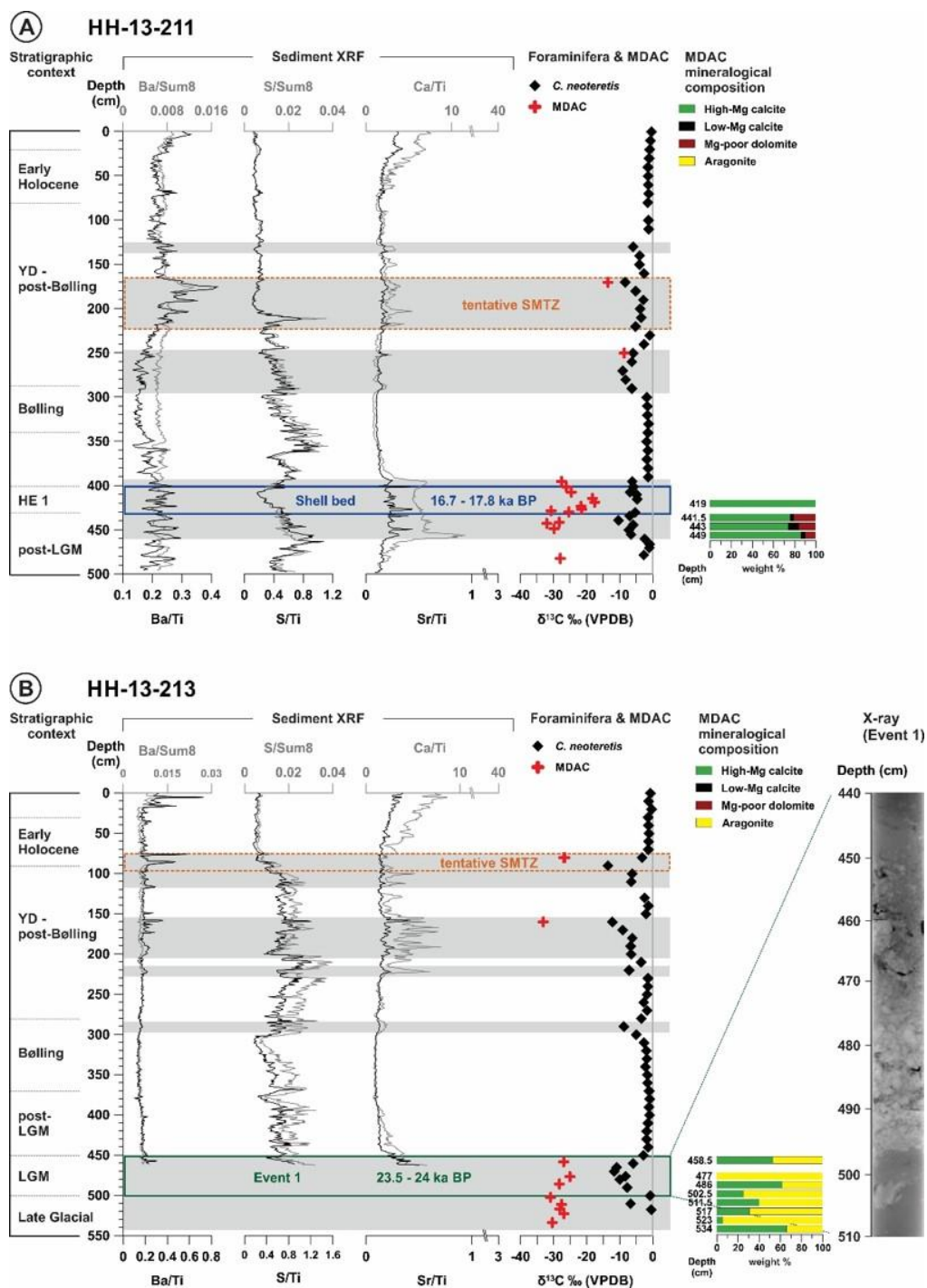
551 **Fig. 5.** Porewater data according to Hong et al. (2016), sediment elemental ratios, $\delta^{13}\text{C}$ of benthic
 552 foraminifera (*C. neoteretis*), and mineralogical composition of the MDAC nodules of **(A)** HH-13-200 and
 553 **(B)** HH-13-203. The orange box indicates the present-day SMTZ as derived from porewater data. Grey
 554 bars indicate negative foraminiferal $\delta^{13}\text{C}$ excursions. Position of the shell bed in HH-13-203 according

555 to Ambrose et al. (2015) (blue box). YD – Younger Dryas. HE 1 – Heinrich Event 1. Ba – Barium. S –
556 Sulphur. Ti – Titanium. Ca – Calcium. Sr – Strontium. Sum8 - sum of the eight most abundant elements
557 in our record. Note varying scales.

558
559 A common approach to determine the present-day SMTZ position is using the mutual depletion of
560 sulphate and methane concentrations in porewater (e.g. Jørgensen and Kasten, 2006). The present-
561 day SMTZ in core HH-13-200 is at 75-115 cm (Tab. 4, Hong et al., 2016; host sediment age ca. 11.4-10
562 ka, Early Holocene, Fig. 5a), and in core HH-13-203 at 100-140 cm (Tab. 4, Hong et al., 2016; host
563 sediment age ca. 13.4-12.4 ka, Allerød interstadial/Younger Dryas, Fig. 5b). From modelling of sulphate
564 reduction rates, Hong et al. (2016) suggest the SMTZ has been stable for 50 (HH-13-203) to 100 years
565 (HH-13-200). Assuming persistent diffuse seepage where the SMTZ remained long enough at the same
566 position, detectable carbonate precipitation in the sediments and on microfossils is likely to occur. In
567 cores where porewater data are absent (HH-13-211 and HH-13-213), we use barium and sulphur
568 elemental ratios to identify the tentative SMTZ position (Fig. 6). Our approach is based on sediment
569 and porewater Ba profiles that depend on sulphate availability as initially described by Torres et al.
570 (1996). According to previous studies (Torres et al., 1996; Dickens, 2001; Sauer et al. 2017), Ba/Ti peaks
571 immediately above increasing S/Ti concentrations are indicative of the SMTZ position, while double
572 Ba-peaks can be caused by recent vertical movement of the SMTZ (Riedinger et al., 2005). In sediment
573 XRF records of core HH-13-200 a sharp peak in Ba and Ba/Ti occurs directly above the present-day
574 SMTZ (Fig. 5a), suggesting the precipitation of diagenetic barite. In HH-13-203, multiple Ba/Ti peaks
575 occur above the present-day SMTZ (Fig. 5b). Sulphur counts in the sediment of both cores are low
576 within and above the SMTZ but increase underneath (Fig. 5), and may reflect increasing amounts of
577 authigenic pyrite (Neretin et al., 2004; Jørgensen and Kasten, 2006).

578 Sediment XRF ratios for Ba/Ti and S/Ti along with foraminifera and MDAC records from cores HH-13-
579 211 and HH-13-213 are presented in Figure 6. In HH-13-211, a prominent Ba/Ti peak is located
580 immediately above a steep rise in S/Ti (Fig. 6a; 165-225 cm). In HH-13-213, the level with multiple Ba/Ti

581 peaks is located directly above a zone with rising S/Ti at the depth of 70-100 cm (Fig. 6b). Indicated by
 582 the largest barium peak and further geological evidence such as MDAC nodules, negative foraminiferal
 583 $\delta^{13}C$ excursions and elevated Sr/Ti ratios at corresponding depth (Fig. 6), the tentative present-day
 584 SMTZ in core HH-13-211 is at 165-185 cm (host sediment age ca. 11.9-12.3 ka, Younger Dryas, Fig. 6a)
 585 while it is at 70-100 cm in core HH-13-213 (host sediment age ca. 10.3-10 ka, Early Holocene, Fig. 6b).
 586



587

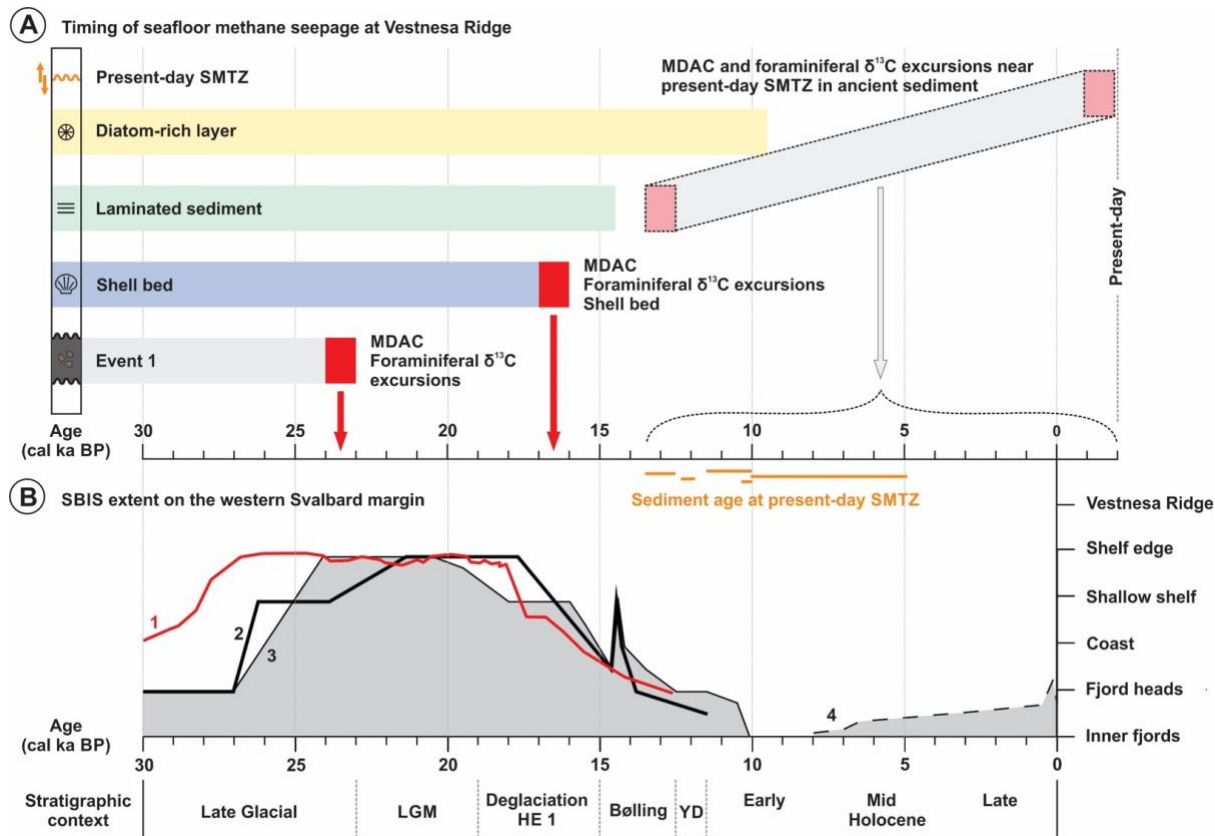
588 **Fig. 6.** Sediment elemental ratios, $\delta^{13}\text{C}$ of benthic foraminifera (*C. neoteretis*) and mineralogical
 589 composition of the MDAC nodules of **(A)** HH-13-211 and **(B)** HH-13-213. The dashed orange box
 590 indicates the tentative SMTZ. Position of the shell bed in HH-13-211 according to Ambrose et al. (2015)
 591 (blue box). Grey bars indicate negative foraminiferal $\delta^{13}\text{C}$ excursions. YD – Younger Dryas. HE 1 –
 592 Heinrich Event 1. Ba – Barium. S – Sulphur. Ti – Titanium. Ca – Calcium. Sr – Strontium. Sum8 - sum of
 593 the eight most common elements in our record. Note varying scales.

594

595 4.4 Timing of past seepage episodes at Vestnesa Ridge

596 Along the Vestnesa Ridge transect, 32 sediment intervals tracking subseafloor methane cycling and/or
 597 seepage episodes occur in the studied cores (Fig. 4b). We observe one major episode that occurred
 598 during the LGM at ca. 24-23.5 ka BP (Event 1) or shortly after, another significant episode coinciding
 599 with the HE 1 (17.7-16.7 ka BP), and multiple isolated episodes in up to 13.4 ka old host sediment (Fig.
 600 7).

601



602

603

604 **Fig. 7. (A)** Timing of methane seepage at Vestnesa Ridge. MDAC nodules, negative $\delta^{13}\text{C}$ excursions in
605 foraminiferal records, and the shell bed document main methane seepage episodes at Vestnesa Ridge
606 in sediments deposited at the LGM, during HE 1, and isolated episodes due to diagenetic methane
607 cycling at vertically migrating SMTZs in younger sediments. **(B)** SBIS extent at western Svalbard during
608 the past 30 ka. LGM – Last Glacial Maximum. HE 1 – Heinrich Event 1. YD – Younger Dryas. Modified
609 from Jessen et al. (2010). SBIS ice extent curves are based on (1): Patton et al. (2015),
610 (2): Elverhøi et al. (1995), (3): Jessen et al. (2010), (4): Svendsen and Mangerud (1997).

611

612

613 Assessing the timing of past methane seepage is challenging since diagenetic alteration by MDAC
614 precipitation is independent from the host sediment age. The precipitation age of aragonite-rich
615 MDAC, which are free of detrital impurities, can be determined using U/Th chronology (Teichert et al.,
616 2003; Bayon et al., 2009; 2013; Crémière et al., 2016b; Sauer et al., 2017). Here, available MDAC
617 nodules are not suitable for U/Th geochronology, and therefore, only their occurrences below the
618 present-day SMTZ can indirectly constrain the timing of subseafloor methane enrichment and
619 methane seepage.

620 Abundant MDAC nodules at the base of core HH-13-213 are restricted to the Event 1 sediments (ca.
621 24-23.5 ka BP; Fig. 6) with high sedimentation rates (S2). We suggest the carbonate precipitation in
622 these LGM sediments occurred syn-sedimentary or shortly post-dating the deposition. This is
623 consistent with the aragonite dominance of the MDAC nodules that implies high methane flux and the
624 SMTZ position very close to the seafloor. Thus, we infer that the oldest episode of subseafloor methane
625 enrichment in this dataset occurred between the SBIS LGM shelf edge glaciation at ca. 24 ka BP (Fig. 7;
626 Hormes et al., 2013; Patton et al., 2015 and references therein) and the deposition of the shell bed.
627 The shell bed (Ambrose et al., 2015; Szybor and Rasmussen, 2017a) is the only directly dated paleo-
628 methane seepage episode from Vestnesa Ridge. Its age (17.7-16.7 ka BP) indicates the shell bed

629 persisted for a period of approximately 1,000 years during HE 1 (Ambrose et al., 2015; Figs. 7; 8). The
630 species composition is typical for bivalves and gastropods that lived partially burrowed at the sediment
631 surface (Ambrose et al., 2015). Furthermore, the mineral composition of the MDAC nodules found
632 within the shell bed in cores HH-13-203 (Fig. 5b) and HH-12-211 (Fig. 6a) suggests that the
633 chemosynthetic bivalve community colonised the former sediment surface. The shell bed occurs in
634 two different pockmarks spaced approximately 2 km apart, but is absent in the area between those
635 pockmarks. The similar species composition and concurring ages suggest the shell bed represents the
636 same biological community. During HE 1 chemosynthetic bivalves recovered from the two different
637 pockmarks document a common methane seepage phase suggesting a regional event.

638 Ongoing methane seepage at Vestnesa Ridge has been under regular observation since 2008 (Hustoft
639 et al., 2009; Bünz et al., 2012; Panieri et al., 2017b) and seems to be persistent for at least a decade.
640 At the western Svalbard margin and Vestnesa Ridge, erosion or non-deposition throughout the
641 Holocene exposes sediments older than 10-9 ka at the seafloor (Elverhøi et al., 1995; Howe et al., 2008)
642 and the present-day SMTZ (in cores HH-13-200; HH-13-203 and JCR211-GC26) occurs in host sediments
643 up to 13.4 ka old (section 4.3; Figs. 5; 6). We suggest that geological evidence for past methane seepage
644 in post-glacial sediments, such as negative foraminiferal $\delta^{13}\text{C}$ excursions, MDAC nodules, and elevated
645 Sr/Ti elemental ratios, do not necessarily correspond to the host sediment age. Those proxies may in
646 reality represent the present-day SMTZ, or SMTZ shoaling in ancient host sediment due to changes in
647 methane fluxes.

648 Our data do not reveal if all methane was consumed via AOM at the SMTZ, or if a fraction of the
649 methane surpassed the SMTZ, left the seafloor sediments, and eventually entered the bottom water.
650 Because of their diagenetic nature, sedimentary proxies indicating paleo-SMTZs may not always
651 correspond to paleo-methane seepage, but instead may represent dynamic vertical SMTZ migration
652 and subseafloor methane cycling in ancient host sediments.

653 From the Lunde and Lomvi pockmarks, high spatial heterogeneity of seepage with diffuse and focused
654 fluid flow has been described by Panieri et al. (2017b). Thus, observations of subseafloor methane

655 enrichment and SMTZ shoaling may suggest weaker, diffuse fluid flow while stronger, focused fluid
656 flow that is currently occurring from pits within the Lunde and Lomvi pockmarks may be analogous to
657 the fluid flow regime during the formation of the shell beds.

658

659 4.5 Seepage drivers

660 Two hypotheses compete about the governing controls on seepage timing at Vestnesa Ridge: 1)
661 Changes in the oceanic thermal regime have the ability to drive gas hydrate dissociation (Szybor and
662 Rasmussen 2017a); and 2) changes in the lithospheric stress regime may result in increased tectonic
663 activity, reactivation of pre-existing faults and fractures, and thus initiating gas migration and seafloor
664 methane seepage (Ambrose et al., 2015; Consolaro et al., 2015; Plaza-Faverola et al., 2015).

665

666 4.5.1 Seepage in response to bottom water temperature (BWT) increase

667 During the LGM, BWTs in the Arctic Ocean and the Nordic Seas have been 2-3°C warmer than Holocene
668 and modern temperatures (Cronin et al., 2012; Thornalley et al., 2015). After SBIS disintegration, the
669 BWT along the western Svalbard margin remained warm due to northward advection of Atlantic water,
670 and probably peaked during HE 1 and the Bølling-Allerød interstadials (Rasmussen and Thomsen, 2004;
671 Rasmussen et al., 2007; Ślubowska-Woldengen et al., 2007; Szybor and Rasmussen, 2017a; Consolaro
672 et al., 2017). This is based on the abundance of warm-water benthic foraminifera and *Vesicomyidae*
673 bivalves, the latter are today most abundant at low latitudes between 30°S and 30°N, and nearly
674 absent at latitudes beyond 60° (Krylova and Sahling, 2010; Hansen et al., 2017). Szybor and Rasmussen
675 (2017a) hypothesize that *Vesicomyidae* may have benefited from warmer BWT at Vestnesa Ridge
676 during HE 1 and propose that, in addition to elevated methane concentrations, warmer BWT during
677 HE 1 may have been a controlling factor on the occurrence of the shell bed.

678 It is unlikely that the available heat energy from elevated BWT during the LGM was adequate to warm
679 up the shallow sediment and dissociate even small-scale near-seafloor gas hydrate accumulations at
680 Vestnesa Ridge, heat propagation through sediments is generally slow (Xu et al., 2001; Taylor et al.,
681 2005; O'Connor et al., 2010; Darnell and Flemings, 2015); in fact it takes about 2000 years for a 2°C

682 positive anomaly to raise the temperature in 100m depth by 1°C. Thus, deeper and larger gas hydrate
683 deposits are unlikely to be immediately affected by the HE 1 BWT increase. Furthermore,
684 chemosynthetic bivalve communities are known to colonize seeps over time scales of decades to
685 centuries (Callender and Powell, 2000; Kiel, 2010; Bowden et al., 2013; Levin et al., 2016). Therefore,
686 we do not support the hypothesis that BWT increase during HE 1 alone was the main reason why
687 methane seepage occurred and chemosynthetic organisms colonised the seep.

688

689 *4.5.2 Effects of glacio-isostatic adjustment (GIA) on methane seepage*

690 The fact that recorded seepage episodes at Vestnesa Ridge are restricted to neither glacial nor
691 interglacial periods suggests that the drivers controlling seepage activity are not strictly related to
692 climatic and/or oceanographic variations, but may involve other Earth system processes. Ambrose et
693 al. (2015) hypothesize that the occurrence of the shell bed was associated with tectonic instabilities
694 such as faulting and fracturing leading to a 1000 years long seepage episode at Vestnesa Ridge. In
695 contrast, Consolaro et al. (2015) suggested the combined effect of sea level rise, elevated
696 sedimentation rate, and isostatic rebound as important factor for seepage modulations at Vestnesa
697 Ridge.

698 In particular, glacio-isostatic adjustment (GIA) accompanying variations in SBIS extent emerges as an
699 alternative explanation for SMTZ migration and seepage on Vestnesa Ridge. Glacio-isostatic
700 adjustment is the viscoelastic response of the Earth`s surface to loading and unloading of the crust due
701 to ice sheet dynamics, which causes two main types of stresses. Vertical stresses occur due to crustal
702 subsidence and displacement of viscous mantle material to the periphery of the load centre during ice
703 sheet growth (Lambeck and Chappell, 2001; Peltier, 2001; Whitehouse 2009; Lund, 2015). The
704 horizontal flexure of the Earth`s crust and increases in the pore fluid pressure can cause fault
705 instabilities and opening of fractures (Hutri et al., 2007; Lund et al., 2011). In addition, the rebound
706 stress (i.e. during deglaciation) can be strong enough to cause slip on faults that are close to failure
707 due to background regional stresses (e.g. Lund et al., 2011 and references therein).

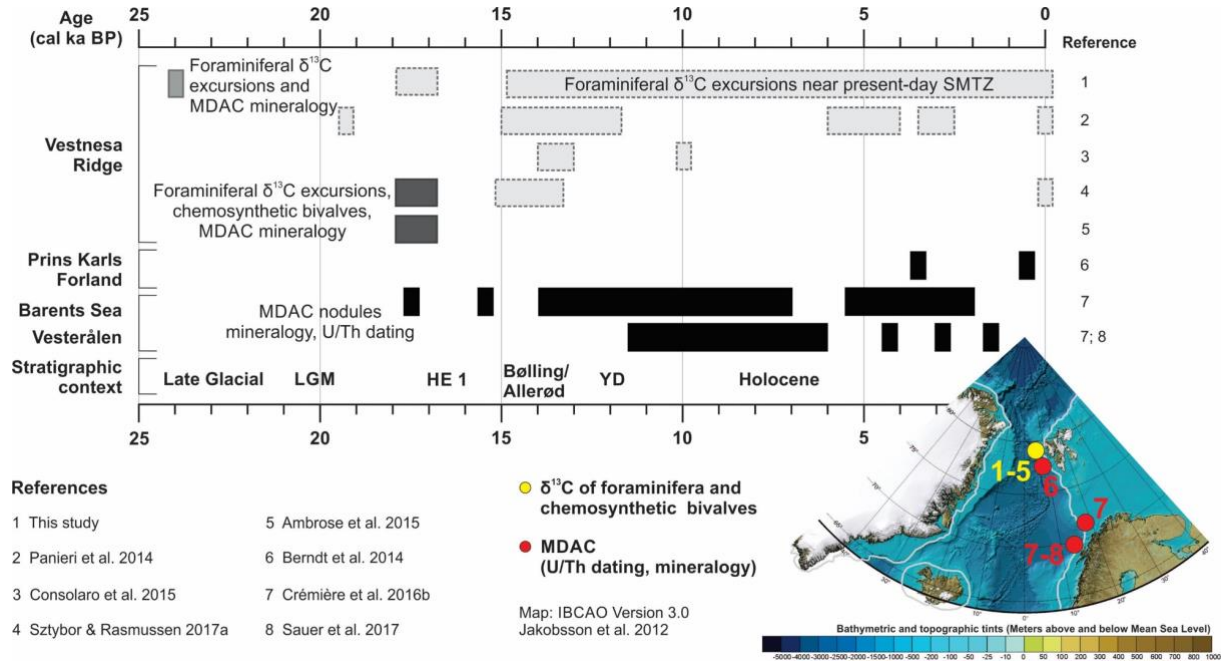
708 Linear high permeability conduits, such as neotectonic faults and fractures, have long been recognised
709 as pathways for fluid migration that is commonly initiated by changes in pore water pressure and/or
710 increased seismicity (e.g. Milkov, 2000; Revil, 2002; Jonsson et al., 2003; Ho et al. 2010; Dupre et al.,
711 2015; Franek et al. 2017). Additionally, a modelling study performed by Klusman and Saeed (1996)
712 suggests gaseous hydrocarbons preferably migrate vertically as buoyant microbubbles along fault
713 systems. For the western Svalbard continental margin, the chemical characteristics of gaseous
714 hydrocarbons suggest vertical migration along re-activated fault systems (Knies et al., 2004). This is
715 consistent with a study from Mau et al. (2017) who report a significant number of gas discharge sites
716 between 74 and 79°N at the western Svalbard continental margin where faults in the underlying rock,
717 such as the Hornsund Fracture Zone, intersect with the seafloor. Although Vestnesa Ridge is located a
718 few kilometres to the west of the shelf break of the western Svalbard continental margin on oceanic
719 crust and in 1200 to 1300 m water depth, GIA at the SBIS periphery could have sparked the re-
720 activation of pre-existing tectonic lineaments at Vestnesa Ridge. During Event 1 when the SBIS reached
721 its maximum extent, vertical and horizontal stresses of GIA may extend over a wide area and thus may
722 have depressed the Earth crust or supported forebulge migration (Lund 2015). Such tectonic
723 movements could have contributed to the opening of fractures and allow fluid migration and methane
724 release during the LGM, and the last deglaciation. The opening of fluid migration pathways may have
725 facilitated subseafloor methane enrichment that lead to shoaling of the SMTZ, shallow subseafloor
726 diagenesis, and/or seafloor methane seepage.

727 Sediments along the ridge have been exposed to complex tectonism (e.g. Crane et al., 2001). Plaza-
728 Faverola et al. (2015) documented sub-seafloor faults and fractures associated with pockmarks on
729 both the active eastern segment and the western inactive segment. Based on differences in the faulting
730 pattern and fault orientation on the eastern compared to the western Vestnesa Ridge segment, the
731 authors postulated that tectonic stress variations along the ridge may control seepage activity. The
732 striking differences between the $\delta^{13}\text{C}$ curves from the core on the north-western Vestnesa Ridge

733 segment (JM10-330, Fig. 4b) and cores from active pockmarks towards the south-east support the
 734 notion of different regional response of Vestnesa Ridge to tectonic processes.

735

736



737

738 **Fig. 8.** Records of methane seepage since the LGM in the Nordic Seas. Light grey box – foraminiferal
 739 $\delta^{13}\text{C}$ excursions and MDAC mineralogy in Event 1 sediments. Light grey boxes with dashed line –
 740 foraminiferal $\delta^{13}\text{C}$ excursions approximately corresponding with the present-day SMTZ position and
 741 assumed vertical SMTZ migration. Dark grey boxes – chemosynthetic bivalves of the shell bed,
 742 foraminiferal $\delta^{13}\text{C}$ excursions and MDAC mineralogy. Black boxes – U/Th geochronology and
 743 mineralogy of MDAC nodules. Bathymetry from IBCAO 3.0 (Jakobsson et al., 2012). Grey line delineates
 744 the LGM extent of the SBIS, Iceland and Greenland Ice Sheets according to Patton et al. (2015).

745

746 Several lines of evidence indicate methane seepage during SBIS retreat and throughout the Holocene
 747 in the Nordic Seas (Fig. 8). Seafloor methane seepage in the south-western Barents Sea Shelf is well
 748 documented in MDAC crusts that formed between 17.5 and 2 ka BP on with the majority of U/Th dates
 749 culminating between 14 and 7 ka BP (Crémière et al., 2016b). At the Vesterålen margin offshore
 750 northern Norway, MDAC reveal methane seepage between 11.5 and 6 ka BP (Crémière et al., 2016b)

751 in response to isostatic rebound, pressure release, gas migration along faults, and bottom water
752 warming after disintegration of the Fennoscandian Ice Sheet. Thus, the seafloor methane
753 enrichment during the LGM and the paleo-seepage episode documented by the shell bed during HE1
754 are likely to be in close relationship with SBIS maximum extent and disintegration in north-western
755 Svalbard.

756 After deglaciation, it takes many thousand years to reach isostatic equilibrium through delayed crustal
757 rebound during which seismicity slowly declines. Glacio-isostatic adjustments are lasting longer than
758 the impact of an ice sheet and thus may cause seismic and tectonic activity initiating fluid flow and
759 seabed seepage long after an ice sheet has vanished. This is documented on Svalbard in raised
760 shorelines throughout the Holocene (Forman et al., 1990; 2004) and earthquake activity along the
761 Norwegian continental margin (Fjeldskaar et al., 2000; Lambeck and Chappell, 2001; Bungum et al.,
762 2005; Lund 2015; Lee, 2009; Olesen et al., 2013). Sauer et al. (2017) obtained ages of 4.4-1.6 ka BP
763 from seafloor MDAC crusts that were found at the Vesterålen margin offshore northern Norway. The
764 authors suggest episodes of increased seismicity at the Lofoten-Vesterålen area are due to remaining
765 GIA movements, that triggered earthquake activity and facilitated methane flux and MDAC
766 precipitation. Furthermore, U/Th-dated MDAC crusts show that methane seepage occurred until 2000
767 years ago at the south-western Barents Sea, and has been ongoing for at least 3000 years offshore
768 western Svalbard where MDAC also precipitated within the past 500 years (Berndt et al., 2014;
769 Crémière et al., 2016b).

770 Although our dataset does not always allow differentiating between methane cycling in Early Holocene
771 host sediment and real paleo-seepage episodes, we cannot exclude seepage during the Holocene on
772 Vestnesa Ridge either. Some of the paleo-SMTZs in our records may indeed capture seepage episodes
773 with similar timing as observed in MDAC in the Barents Sea and at the Norwegian continental margin.
774 Glacial isostatic adjustment is an integral component of the Earth system and acts on geological time
775 scales. Compelling evidence complements the hypothesis that GIA sparked tectonic activity and fault
776 re-activation also offshore western Svalbard, may have enabled fluid migration, seafloor methane

777 enrichment, and seafloor methane seepage at Vestnesa Ridge during SBIS disintegration.
778 Diagenetically altered foraminiferal tests, MDAC, sediment geochemical records, and chemosynthetic
779 fauna suggests that shallow subseafloor methane cycling and seafloor methane seepage at Vestnesa
780 Ridge may respond to long-term changes in Earth system processes (Dickens, 2003; Hong et al., 2017,
781 Wallmann et al. 2018).

782

783 5 Conclusions

784 We have established a stratigraphic framework for the sediments along Vestnesa Ridge using
785 the existing stratigraphic marker horizons defined for the western Svalbard margin between 76 to
786 80°N. Our data are consistent with the $\delta^{18}\text{O}$ stratigraphy for planktic foraminifera from the north-
787 western Svalbard margin during the Last Glacial Maximum (LGM), deglaciation, and Early
788 Holocene, and thus provide an important chronological framework for stratigraphic correlation
789 and interpretation of methane-related diagenetic processes.

790 Shallow subseafloor methane cycling and seafloor seepage cover the complete time span since
791 the LGM and disintegration of the Svalbard-Barents Sea Ice Sheet (SBIS), and are documented in
792 multiple proxies (negative foraminiferal $\delta^{13}\text{C}$ excursions, MDAC nodules, elevated Sr/Ti elemental
793 ratios, chemosynthetic bivalves). Seafloor methane seepage occurred during the LGM (24-23.5 ka
794 BP) and Heinrich Event 1 (HE 1, 17.7-16.7 ka BP).

795 Sedimentary proxies indicating paleo-SMTZs do not always correspond to seafloor methane
796 seepage but instead may indicate shallow subseafloor methane cycling and SMTZ shoaling. Such
797 paleo-SMTZ's may be formed in the subsurface and do not necessarily correspond to the host
798 sediment age. Indications of methane seepage other than during LGM, HE 1, and at the present-
799 day SMTZ possibly represent weaker methane flux since the sediment deposition until today.

800 Although the influence of elevated bottom water temperatures on seafloor methane seepage
801 cannot be excluded, we consider glacio-isostatic adjustments as most important factor controlling
802 past and ongoing methane seepage and shallow subseafloor methane cycling on Vestnesa Ridge.

803 The build-up and disintegration of major ice sheets is accompanied by crustal isostatic adjustments
804 and increased seismicity. Glacio-isostatic adjustments may have triggered the re-activation of
805 tectonic lineaments at Vestnesa Ridge and thus could have provided fluid migration pathways.

806

807

808 6 Acknowledgements

809 This work was supported by the Research Council of Norway through its Centre of Excellence funding
810 scheme for CAGE, project number 223259, and partially by the NORCRUST project, grant
811 number 255150. Parts of the isotopic analyses were supported by the PNRA (Italian National Antarctic
812 Program) Project FORMAT. We thank the captain, crewmembers and scientific team of *R/V Helmer*
813 *Hanssen* for their contribution during the research cruises CAGE-2013 and CAGE-2014. We are
814 indebted to Stefan Bünz who acquired 3D seismic data from the Vestnesa Ridge and facilitated
815 bathymetry maps for the study area. AS obtained a travel grant from the Norwegian Research School
816 in Climate Dynamics (ResClim). The manuscript benefited from editing and language correction by
817 Monica Winsborrow and Hanne-Kristin Paulsen.